JGR Solid Earth

RESEARCH ARTICLE
10.1029/2019JB017418

Key Points:
- Yields of six North Korean underground nuclear tests are estimated by modeling high-frequency (>4 Hz) teleseismic *P* wave amplitudes
- Waveform equalization of short-period teleseismic *P* and regional *Pn* seismograms provides yield and depth estimates for all six events
- Spectral ratios of broadband regional *Pn* signals at station MDJ validate the six explosion source models from waveform equalization

Supporting Information:
- Supporting Information S1
- Table S11

Correspondence to:
T. Lay,
tlay@ucsc.edu

Citation:
Voytan, D. P., Lay, T., Chaves, E. J., & Ohman, J. T. (2019). Yield estimates for the six North Korean nuclear tests from teleseismic *P* wave modeling and intercorrelation of *P* and *Pn* recordings. *Journal of Geophysical Research: Solid Earth*, *124*. https://doi.org/10.1029/2019JB017418

Received 21 JAN 2019
Accepted 18 APR 2019
Accepted article online 25 APR 2019

Yield Estimates for the Six North Korean Nuclear Tests From Teleseismic *P* Wave Modeling and Intercorrelation of *P* and *Pn* Recordings

Dimitri P. Voytan[1], Thorne Lay[1], Esteban J. Chaves[2], and John T. Ohman[3]

[1]Department of Earth and Planetary Sciences, University of California Santa Cruz, Santa Cruz, CA, USA, [2]Volcanological and Seismological Observatory of Costa Rica, Universidad Nacional (OVSICORI-UNA), Heredia, Costa Rica, [3]Cooperative Institute for Research in Environmental Sciences, University of Colorado Boulder, Boulder, CO, USA

Abstract The yields of the six declared underground nuclear tests at the North Korean test site are estimated using high-frequency teleseismic *P* wave amplitude modeling and waveform equalization of short-period teleseismic *P* waves and regional *Pn* signals. Average amplitudes of the first cycle of high-frequency (>4 Hz) filtered *P* wave displacements for each event, adjusted for station sampling relative to the 3 September 2017 event, are modeled using Mueller-Murphy explosion source models for granite and a constant-*Q* attenuation operator with $t^* = 0.78 \pm 0.03$ s. The yield estimates range from 2.6 to 230 kt. Intercorrelation, a waveform equalization procedure that accounts for source function and depth-phase variations between events, is applied to large sets of filtered (>0.8 Hz) teleseismic *P* and regional *Pn* seismograms. Searching over yield and burial depth for both events gives optimal parameters by simultaneous waveform equalization of multiple stations. Using specified burial depths spanning from 430 to 710 m for all events based on estimated locations in the source topography assuming tunneling with 4% grade, along with allowing for reduction in source region velocity due to weathering, rock layering, and damage zones, gives yield estimates ranging from 1.4 to 250 kt. Comparison of predicted and observed spectral ratios of *Pn* phases at station MDJ establishes that these source models are reasonable. Using the preferred yield estimates from intercorrelation, W_{IC}, a yield-calibrated relation of $m_{bNEIC} = 0.9 \log_{10} W_{IC} + 4.13$ is determined for the North Korean test site.

1. Introduction

During 2006 to 2017, the Democratic People's Republic of Korea (DPRK) conducted six declared underground nuclear tests (Table 1) at the Punggye-ri test site near 41.3°N, 129.1°E. Seismological monitoring is the primary method for remotely detecting, locating, identifying, and estimating explosion yields of underground nuclear tests. The events were readily detected and identified (e.g., Walter et al., 2018), in addition to being announced. Precise relative locations for the six explosions, with uncertainties on the order of a few hundred meters, have been determined by numerous seismic differential arrival time studies (e.g., Carluccio et al., 2014; Gibbons et al., 2017, 2018; He et al., 2018; Myers et al., 2018; Murphy et al., 2013; Selby, 2010; Wang et al., 2018; Wen & Long, 2010; Yao et al., 2018; Zhang & Wen, 2013; Zhao et al., 2016; Zhao, Xie, He, et al., 2017). Absolute locations are much more difficult to resolve, and various strategies have been used to place the suite of precise relative locations in absolute position with respect to the source region topography, locations of tunnel portals, and/or deformation features on the surface inferred from InSAR or satellite photography (e.g., Murphy et al., 2013; Myers et al., 2018; Pabian & Coblentz, 2018; Pabian & Hecker, 2012; Patton & Pabian, 2014; Wei, 2017), with recent results having less than ~0.5-km variations. The absence of collapse craters for all events complicates the absolute location process and indicates that burial depths for most events significantly exceed what is required for containment. The representative epicenter estimates listed in Table 1 from Myers et al. (2018) are spatially constrained by modeling 3-D surface deformation indicated by InSAR to specify the location of NK4. The preponderance of the evidence favors locations of the 2006 explosion beneath a ridgeline northeast of an eastern portal and of the other five events north-northwest of a western portal below the southern slope or summit ridge of Mount Mantap (Figure 1). The mountain peak ridge elevation is 2,205–2,240 m, 776–800 m higher than the western portal entrance.

Table 1
Nuclear Test Origin Time and Body Wave Magnitudes (m_b) From the USGS National Earthquake Information Center (NEIC) and the Comprehensive Test Ban Treaty Organization (CTBTO), Epicentral Locations From Myers et al. (2018), and Abbreviated Event Name Used in This Paper for the Six DPRK Nuclear Tests

Event Time, UTC	m_{bNEIC}	m_{bCTBTO}	Latitude (°N)	Longitude (°E)	Event name
9 October 2006 01:35:28.00	4.3	4.1	41.29192	129.10907	NK1
25 May 2009 00:54:43.12	4.7	4.5	41.29654	129.08298	NK2
12 February 2013 02:57:51.49	5.1	4.9	41.29276	129.07851	NK3
6 January 2016 01:30:01.48	5.1	4.9	41.29932	129.07622	NK4
9 September 2016 00:30:01.44	5.3	5.1	41.29983	129.08157	NK5
3 September 2017 03:30:01.77	6.3	6.1	41.29999	129.07901	NK6

Given that the DPRK explosions were conducted in tunnels in mountainous topography, their effective burial depths were controlled by unknown tunnel geometry relative to observed portal locations. Smaller tunnel explosions can readily be significantly overburied relative to normal containment practices. Burial depth affects the confining pressure around the shot point such that an overburied explosion with larger yield can produce the same seismic motions as a lower-yield explosion at (shallower) normal burial depth. Thus, for precise estimation of explosion yields, determination of the burial depth is important. The estimates of source epicenters relative to the topography (Figure 1) place bounds on the plausible burial depths. Assuming a positive tunnel grade of ~4%, which would ensure drainage (Pasyanos & Myers, 2018; Sinha, 1991), inferred topographic differences require correction of up to ~80 m to provide correct vertical depths, and surface slope may further reduce the minimum distance from the free surface. Estimation of depth-phase arrival times from surface reflections can more directly constrain the source depth (Murphy et al., 2013) as can absolute modeling of three-dimensional surface deformation (e.g., Myers et al., 2018; Wang et al., 2018). The ranges of published source depth estimates distribute from 200 to 800 m for the six events (Table 2 and Table S1 in the supporting information).

Determining accurate absolute yield estimates from seismic recordings also requires knowledge of the emplacement medium properties (source region rock type, water table level, etc.), as these affect the cavity size, seismic coupling, and yield scaling, along with the elastic structure and attenuation properties of the

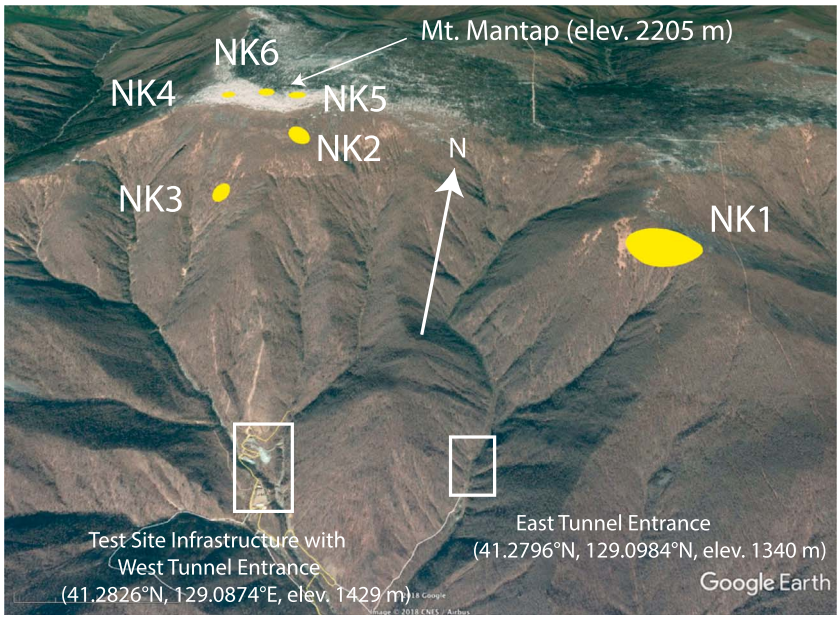

Figure 1. Google Earth image of the Democratic People's Republic of Korea test site looking down from south-southeast of Mount Mantap. The estimated location uncertainty areas (95% probability) of the six North Korean tests obtained by Myers et al. (2018; Table 1) are shown by the yellow regions. The location of the tunnel entrances for the eastern and western tunnels are within the white boxes. Estimates of tunnel entrance locations and elevations are from Coblentz and Pabian (2015). The distance from the center of the NK1 probability ellipse to that for NK3 is 2.57 km.

Table 2
Summary Ranges for Published Estimates of Yield and Depth of Burial From Various Studies

	Range of estimated yields and burial depths	
Event name	Depth of burial (m)	Yield (kt)
2006 (NK1)	200–600	0.5–2.0
2009 (NK2)	300–710	1.0–10.5
2013 (NK3)	320–700	7.5–32.5
2016a (NK4)	420–783	2–24.4
2016b (NK5)	476–800	3–115
2017 (NK6)	450–800	30–300

Note. Details are provided in the supporting information Table S1.

crust and upper mantle along each path from the source to recording stations. Synthesizing existing small-scale geologic maps with topographic information, specifically the pattern of drainages within the region, Coblentz and Pabian (2015) conclude that Mount Mantap is composed of either a Mesozoic/Cretaceous diorite or a Mesozoic granite and overlain by stratified volcanics and a thin basalt cap layer. The site of the 2006 event, ~2 km to the east, differs in that the rock in this region is likely highly fractured and near the eastward extent of a granite-gneiss contact (Coblentz & Pabian, 2015). Specific rock properties at the explosion source depths are not known. One can estimate various relative explosion size measures with high precision by virtue of using consistent measurements on common source-to-station paths and thereby suppressing unknown propagation effects, but inferring relative or absolute yields still requires knowledge of the source model and its scaling. Given that only a tiny fraction of the energy release in a nuclear explosion generates elastic waves that can be seismically recorded (e.g., Haskell, 1967), empirical calibration using independently measured explosions yields and seismic measures such as short-period *P*-wave magnitude, m_b, is ultimately required for high-confidence yield determinations for any test site. Lacking direct determination of any of the DPRK yields, all estimates involve multiple assumptions for which the uncertainties must be considered.

A variety of methods have been used to estimate the yields or seismic moments of the six tests, including assumed transportability of body wave, surface wave, or *Lg* magnitude yield scaling relations (e.g., Chun et al., 2011; Hartmann et al., 2016; Yao et al., 2018; Zhang & Wen, 2013; Zhao et al., 2008, 2012, 2014, 2016, Zhao, Xie, Wang, et al., 2017,Zhao, Xie, He, et al., 2017); modeling of surface deformation (Wang et al., 2018; Wei, 2017), regional waveforms and spectra (e.g., Murphy et al., 2013; Rougier et al., 2011; Stevens & O'Brien, 2018; Stroujkova, 2018; Wang et al., 2018), regional coda envelopes (e.g., Pasyanos & Myers, 2018), network-averaged teleseismic *P* wave spectra (e.g., Murphy et al., 2013), and teleseismic *P* waveforms (e.g., Chaves et al., 2018; Ni et al., 2010); and moment tensor inversion for the total and isotropic moment of the explosions (e.g., Alvizuri & Tape, 2018; Barth, 2014; Cesca et al., 2017; Chiang et al., 2018; Ford et al., 2009; Ichinose et al., 2017; Liu, Li, Zahradnik, Sokos, Liu, et al., 2018,Liu, Li, Zahradník, Sokos, & Plicka, 2018; Vavrycuk & Kim, 2014; Wang et al., 2018; Yao et al., 2018). Some depth constraints are inferred from infrasound as well (Assink et al., 2016). We summarize the ranges of yield estimates from the literature in Table 2, with details provided in Table S1.

Guided by these prior studies, we estimate the yields of the six DPRK nuclear tests using both absolute and relative methods. We first model teleseismic average absolute amplitudes of the first cycle of high-frequency (>4 Hz) filtered *P* displacement waveforms, which are relatively insensitive to depth-phase interference, but are sensitive to the choice of source model (including its depth dependence) and path attenuation. We then use a short-period waveform equalization method that provides relative source strength estimates and source depth estimates for an assumed source model parameterization (Burger et al., 1986; Lay, 1985; Lay et al., 1984). Associated absolute yield estimates are based on baselines from the waveform modeling, and our preferred yield estimates from intercorrelation specify the source depths to stabilize the waveform equalization. For the uncalibrated DPRK test site, the estimates of yield obtained here involve assumptions of specific source rock properties, a specific explosion source model with associated scaling properties, and specific elastic and anelastic structures; all of these have uncertainties and the yield estimates are thus largely self-consistent, but nonunique.

2. Data Processing

Vertical-component regional and teleseismic *P* wave recordings from all stations (>2,500 for 2017) in the Incorporated Research Institutions for Seismology (IRIS) database are used in this study. The highest sample rate and best signal-to-noise ratio data from BHZ, SHZ or HHZ channels are selected. For analysis of high-frequency *P* wave signals at teleseismic distances, the preferred channels are deconvolved by the instrument response to produce ground displacements in the passband 0.1 to 5 s, filtered with a causal high-pass Butterworth fourth-order filter with a corner of 4-Hz, and then interpolated to time sampling of 0.01 s, if

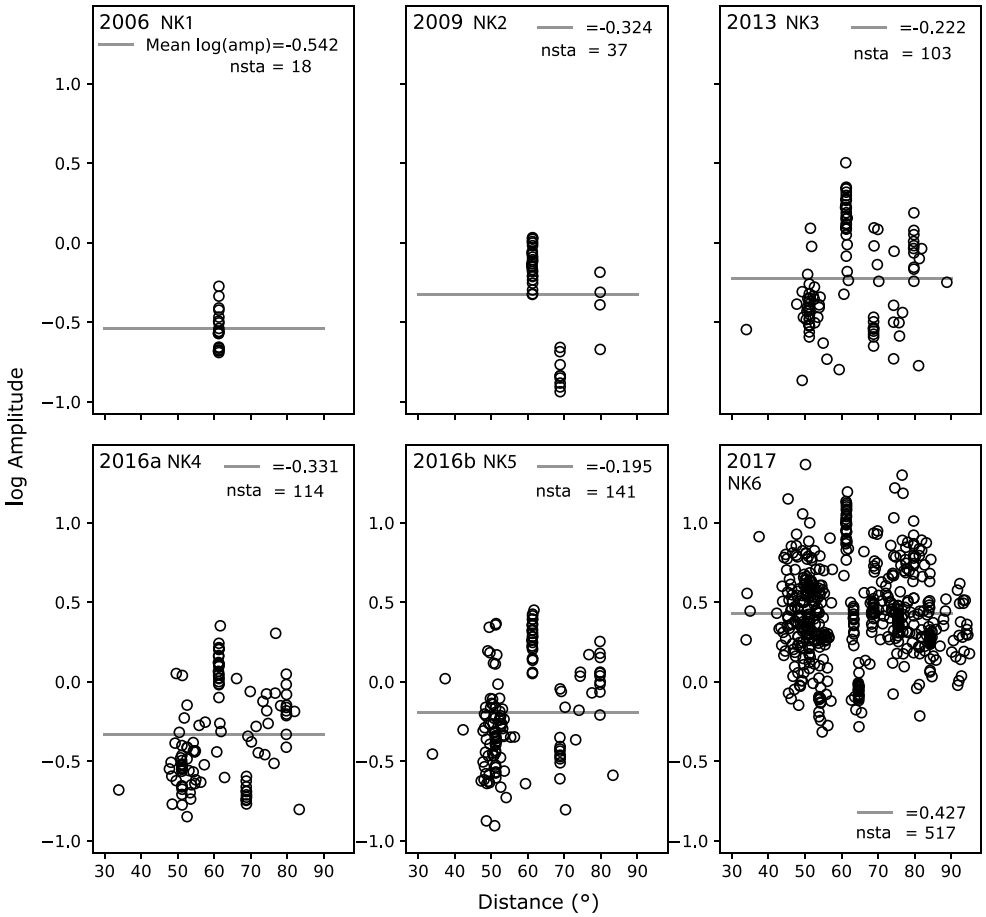

Figure 2. Logarithmic amplitudes of first-peak-to-first-trough of teleseismic *P* wave ground displacements filtered with a causal fourth-order high-pass Butterworth filter with a corner frequency of 4 Hz, corrected for geometric spreading to a reference distance of 5,500 km, plotted as a function of epicentral distance from the source region for the six North Korean underground nuclear tests. The log-averaged mean values in nanometer are 0.287, 0.474, 0.600, 0.467, 0.638, and 2.676 for NK1–NK6, respectively. These mean values are biased by censoring of low-amplitude signals for the smaller events.

necessary. This processing is the same as that performed for NK6 data in Chaves et al. (2018). For short-period teleseismic *P* wave relative waveform analysis, the instrument responses are not deconvolved, and the signals are just filtered with a causal high-pass fourth-order Butterworth filter with corner of 0.8 Hz, then interpolated to time sampling of 0.01 s. Instrument responses are equalized to September 2017 responses if they changed during the time interval spanned by the explosions. Regional *Pn* recordings at stations other than MDJ are filtered with a high-pass filter with corner of 1.0 Hz. The entire data set is manually screened to exclude traces with poor signal-to-noise ratio. The arrival times of *Pn* and *P* in the high-frequency ground motions and filtered short-period signals are manually picked and 5-s duration time windows extracted.

3. Four-Hertz Amplitude Modeling

For each 4-Hz filtered *P* wave ground displacement signal, the first-peak-to-first-trough amplitude is measured. These amplitudes are corrected for geometric spreading to a reference distance of 5,500 km using a smoothed amplitude-distance curve obtained by ray tracing in a Jeffreys-Bullen Earth model. This provides 18, 37, 103, 114, 141, and 517 amplitude measures for NK1 to NK6, respectively (Figure 2), with the large variation in number of available data reflecting the range of explosion magnitudes (Table 1). The time difference from the first-arrival onset to the first trough in the 4-Hz filtered data is ~0.25 s, primarily controlled by the high-pass filter corner. This is on the order of the expected teleseismic *pP* delay time for burial depths near 700 m for granite source rocks with a *P* velocity, *V*5.5 km/s. These high-frequency measurements are

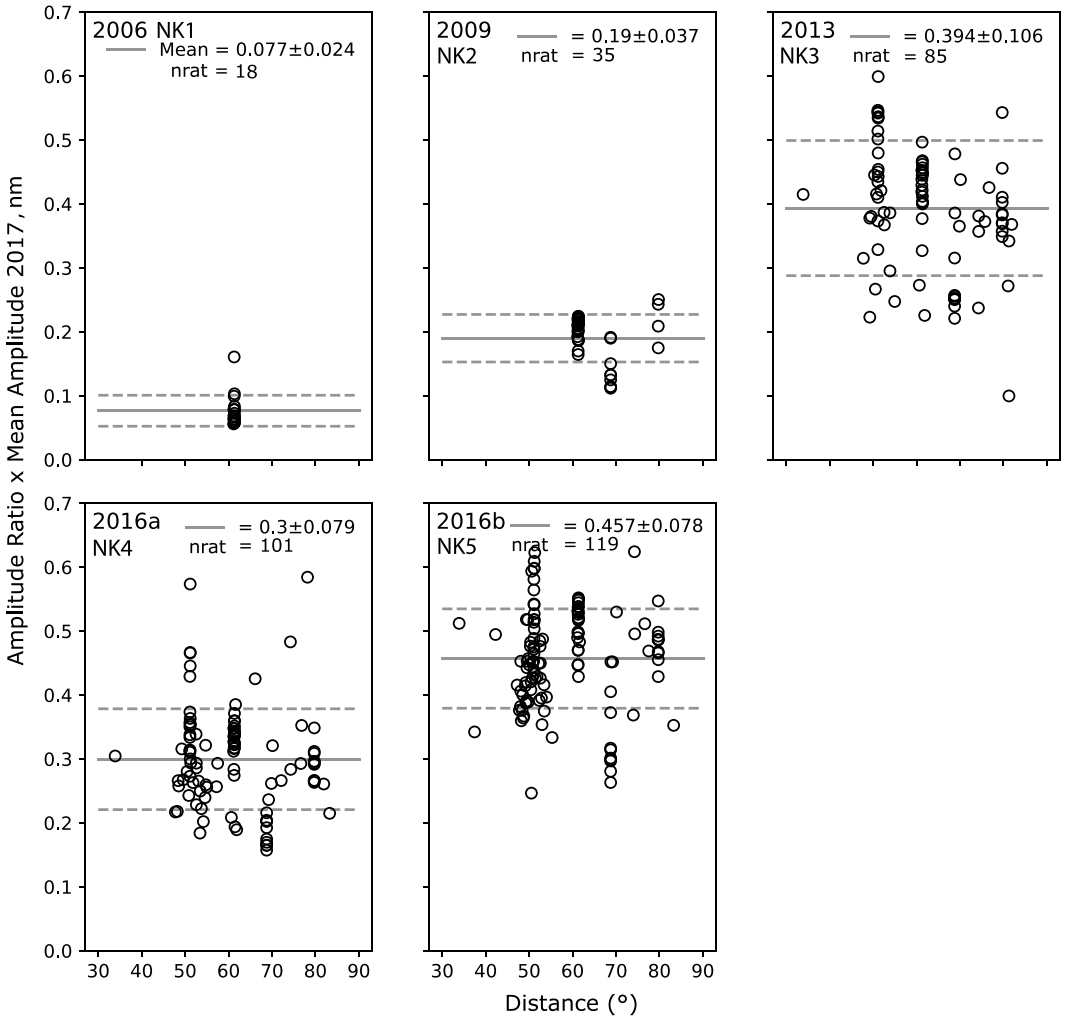

Figure 3. Ratio of observed 4-Hz filtered *P* wave ground displacements for each event relative to the corresponding station observation for event NK6 (2017), with the ratios being multiplied by the mean amplitude (2.676 nm) for NK6. The solid line is the mean scaled ratio, and the dashed lines indicate 1 standard deviation of the scaled ratio values. The *nrat* is the number of stations in common with NK6 for which ratios are shown. The mean values are relatively unbiased estimates relative to NK6 compared to the event averages shown in Figure 2.

thus largely, but not totally, insensitive to interference from the depth phase, as four of the six events are buried deeper than ~600 m. The two shallower events (NK1 and possibly NK3) are likely to have greater *pP* sensitivity in the 4-Hz passband. Since the filter does allow some lower-frequency energy into the signal, all events will have at least minor influence of *pP*. The logarithmically averaged mean amplitudes range over a factor of 9.3 between NK1 and NK6, but Figure 2 indicates that this is an underestimate of the true relative strength of the events, because the data from 2006 are all from relatively high amplitude recordings at the Warramunga Array in Australia, for which the corresponding data for 2017 are significantly higher than that event's population mean (likely due to low upper mantle attenuation beneath Warramunga's continental shield location). Similar sampling biases afflict seismic magnitudes from the National Earthquake Information Center (NEIC; Table 1) due to large differences in numbers of measured station magnitudes, which range from 11 for NK1 to 941 for NK6.

In order to suppress the sampling bias of the mean amplitudes, we compute ratios of the observations for each station recording NK1 to NK5 to the corresponding measurement for the extremely well-sampled NK6. This eliminates the common path and receiver effects, giving less-biased relative amplitude measures. We then multiply each ratio by the logarithmically averaged mean peak-to-trough amplitude for NK6 (2.676 nm) from Figure 2, computing the mean and standard error of the scaled ratios (Figure 3). The

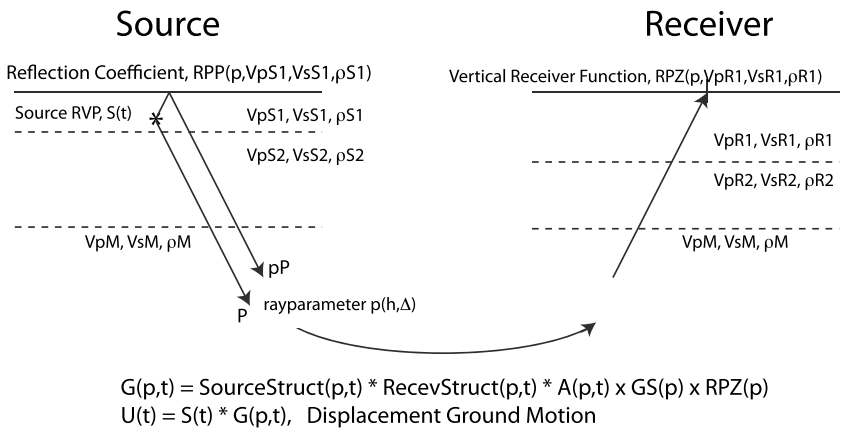

Figure 4. Schematic of the waveform modeling procedure. Far-field ground displacement, $U(t)$ is computed by convolution of the source time function, $S(t)$, and an anelastic Green's function, $G(p,t)$. The source function, $S(t)$, is the reduced velocity potential for the Mueller-Murphy source in a granite medium for a specified yield and source depth. A layered or half-space elastic medium is prescribed and the far-field explosion impulse response is computed with the source structure effects (*SourceStruct*(p,t)) including direct P and surface reflected pP phases computed for ray parameters, p, corresponding to a specific station distance. Geometric spreading, $GS(p)$, depends on mantle or half-space P wave velocity, V_{pM}, S wave velocity, V_{sM}, and density, ρ_M and is computed by ray tracing in a Jeffreys-Bullen earth model. $A(p,t)$ is the attenuation operator, which is a constant-Q Futterman (1962) operator. The receiver function $RPZ(p)$ is computed either for the half-space or for a layered crustal model response (*RecevStruct*(p,t)).

number of ratios is 18, 35, 85, 101, and 119 for NK1 to NK5, respectively. There is now a factor of 34.8 between the mean amplitude estimates for NK1 and NK6, with the increase roughly corresponding to the average bias between Warramunga observations and the event mean for NK6. Normalizing by the mean measure for NK6 provides absolute 4-Hz amplitude measures that are tied to the large data population for NK6. The NK6 mean amplitude for data corrected to 5,500-km distance was modeled jointly with broadband P wave observations by Chaves et al. (2018), resulting in a yield estimate of 230 $\pm$ 50 kt for NK6, for an average constant-Q attenuation parameter $t^* = 0.78 \pm 0.03$ s, where t^* is the path (s) integral $\int ds/[V_p(s)Q(s)]$, or total travel time over path average Q factor. The range of estimated t^* is an approximation of the standard error of the specific data ensemble used for NK6; individual path values of t^* likely vary by ~ $\pm$0.4 s around the central value. The amplitude ratio procedure enables self-consistent modeling of all of the mean scaled ratios using the same attenuation operator.

The modeling procedure used for the 4-Hz amplitudes is schematically illustrated in Figure 4. The far-field response, which includes the pP surface reflection depth phase, is computed for an explosion source impulse at a specified depth in either in a plane-layered or half-space source structure for the ray parameter for a distance of 5,500 km. Geometric spreading is applied, along with a receiver function for either a half-space or layered receiver structure. All of the results presented in this paper are for half-space calculations, given that details of the source structure are not known and simple layered models give very similar results to the half-space calculations. The source time function is the reduced velocity potential (RVP) for far-field P waves, for which we adopt the Mueller-Murphy model (Mueller & Murphy, 1971). This is parameterized by yield and burial depth for a given rock type (e.g., Stevens & Day, 1985; Walter & Priestley, 1991). Here we adopt the empirical granite explosion source parameters specified by Stevens and Day (1985), P velocity, V5.5 km/s, S wave velocity, $V_S = 3.175$ km/s, and density, $\rho = 2{,}550$ kg/m^3. The elastic response is convolved with an attenuation operator; we use a frequency-independent, constant t^* operator (Futterman, 1962). Spectral amplitudes generated by the source, $S(f)$, are strongly affected by t^*, with the ground displacement frequency spectra, $U(f) \propto S(f) \times e^{-\pi f t^*}$. Variation of t^* from path to path clearly exists, but current aspherical attenuation models are not reliable for predicting path-specific values. Thus, we rely on the very large data set for NK6 to provide sufficient sampling of path variations that the mean amplitude can be modeled by an average t^* representative of the overall distribution of path t^* values. Synthetic P wave ground motions are then filtered with the same high-pass Butterworth filter as applied to the data in order to compare the first-peak-to-first-trough 4-Hz amplitude predictions.

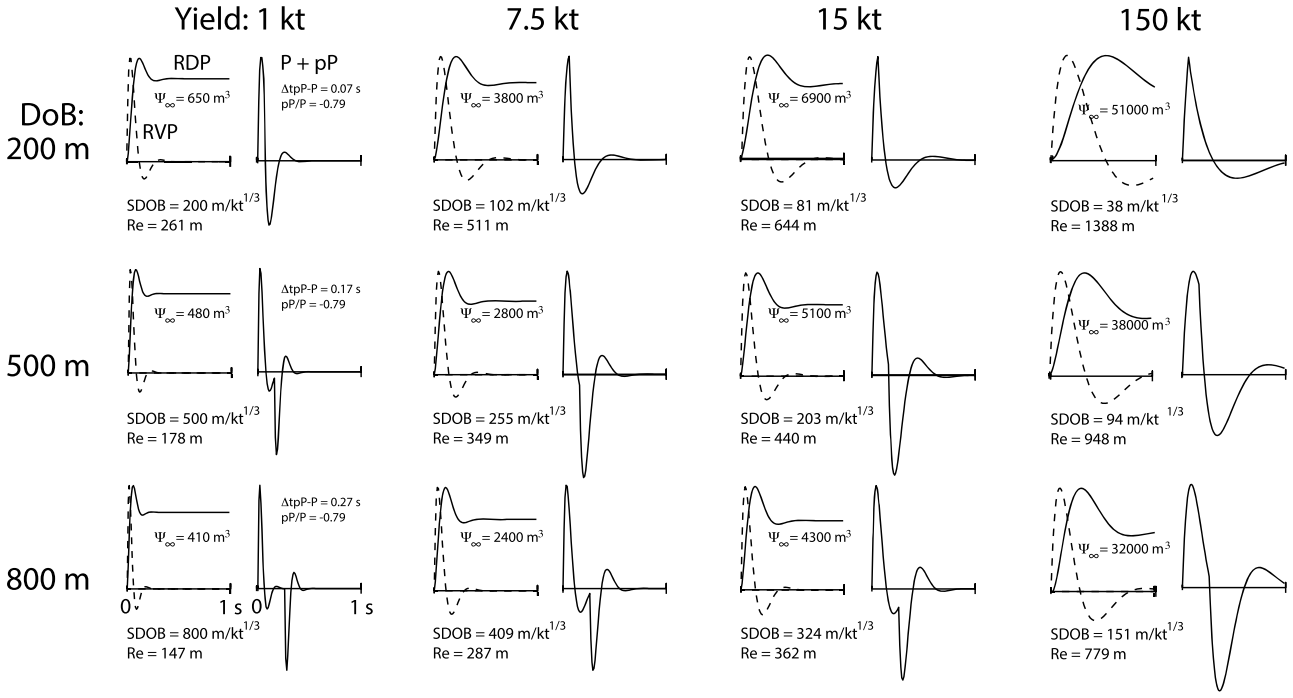

Figure 5. The time domain reduced displacement potential (RDP), reduced velocity potential (RVP), and effective source function (convolution of the RVP and the source region elastic propagation Green's function), for the Mueller-Murphy granite source model for varying depth of burial (DOB) and explosion yield. The corresponding scaled depth of burial (SDOB) and elastic radius, *Re*, and the *pP–P* differential arrival time ($\Delta t_{\mathrm{pP\text{-}P}}$) and *pP/P* amplitude ratio are shown for each case.

The Mueller-Murphy model reduced displacement potential (RDP) and RVP have analytic time domain formulations (Saikia, 2017), as needed for waveform modeling. Figure 5 displays the variation in RDP, RVP, and far-field half-space effective source functions for varying combinations of specified yield and burial depth. The source RDP has moderate overshoot, which produces overshoot in the RVP. The pulse width of the RVP decreases with increasing burial depth, producing complex interference with the negative amplitude *pP* arrival that has the indicated half-space lag time relative to *P* ($\Delta t_{pP\text{-}P}$) and relative amplitude *pP/P*. These source functions will be further smoothed by attenuation and modified by high-pass filtering in order to compare with data, and there are complex tradeoffs between *t**, yield, and, to a lesser extent, burial depth that must be evaluated.

For the 4-Hz modeling procedure we first select an estimate of burial depth for each event, and then compute a broad suite of synthetics for varying yield and *t** combinations. Based on the published estimates of burial depths in Table 2, we specify depths of 380 m for NK1, 600 m for NK2, 420 m for NK3, and 750 m for NK4, NK5, and NK6. These depths are generally consistent with absolute estimates from precise relative location estimates (e.g., Gibbons et al., 2017; Pasyanos & Myers, 2018), but significant uncertainty remains, and we will evaluate the effect of these choices. Filtered synthetics for a distance of 5,500 km are then constructed for the chosen source depth for a range of yield spanning the estimates in Table 2 along with Futterman *t** values from 0.4 to 1.3 s. While some paths likely have frequency-dependent attenuation, Chaves et al. (2018) found that overall their waveform predictions of the NK6 event favored a constant-*Q* model.

The mean and standard deviation of the scaled 4-Hz amplitudes for each event define a trajectory in the *t** yield modeling domain, with lower *t** being required for a lower yield in order to match the observed value. Figure 6 shows the trajectories of the data ($\pm 1\sigma$) superimposed on contours of corresponding amplitude measures for the synthetics for each event. Given our scaling of all amplitude ratios relative to the NK6 event mean that we adopt the preferred *t** value (0.78 $\pm$ 0.03 s) from Chaves et al. (2018) to determine self-consistent absolute yield estimates for each of the six DPRK tests (Table 3), defining generous uncertainty bounds based on the uncertainty range of *t** and the standard deviations of the amplitude measures. These estimates provide reasonable constraints on the range of yields given uncertainties in data

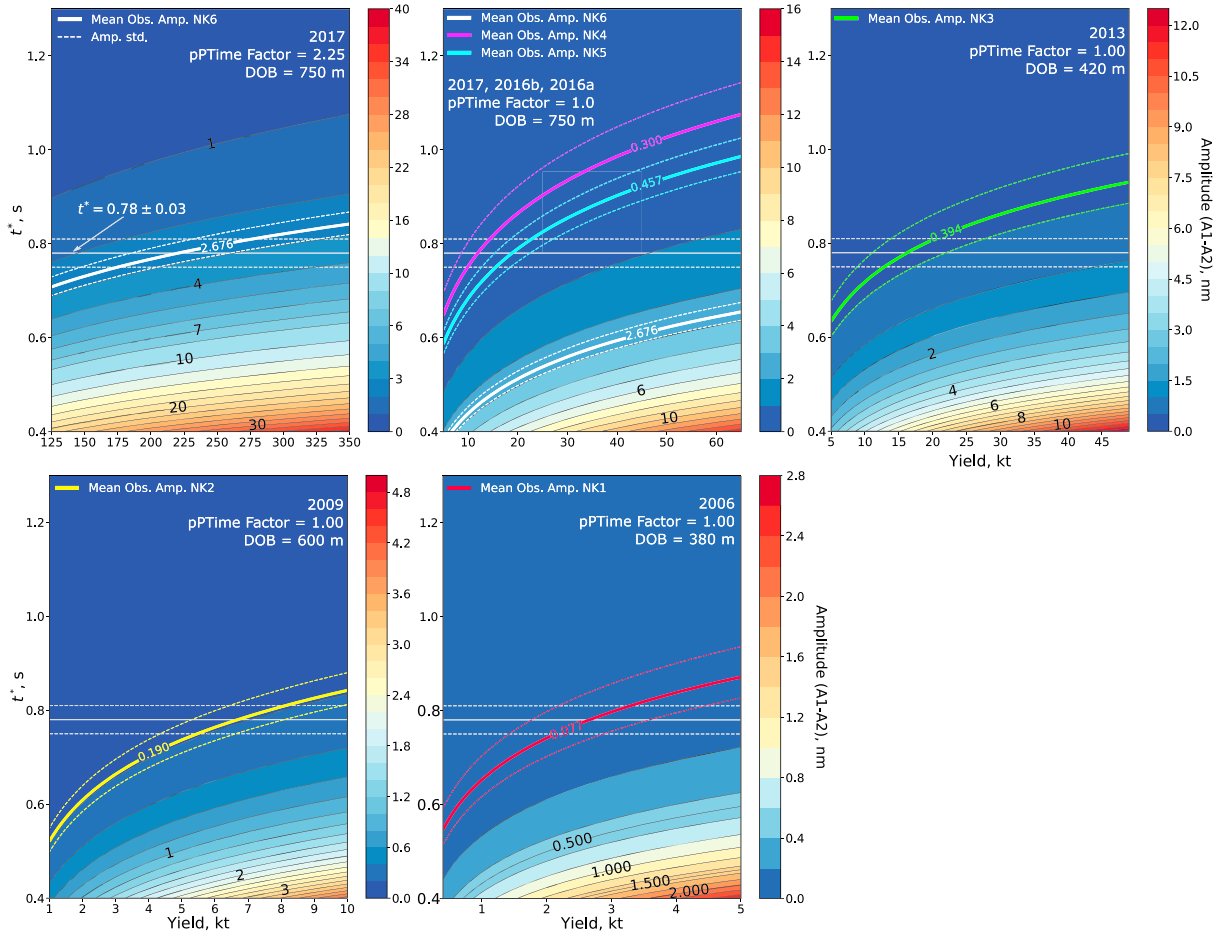

Figure 6. Comparison of observed 4-Hz mean first-peak-to-first-trough *P* displacement amplitudes and their uncertainty ranges (colored curves) for the six North Korean nuclear tests with predictions from identically filtered synthetics for large ranges of attenuation operator *t** and explosion yield using Mueller-Murphy granite source models. The predictions are for the indicated specific depth of burial (DOB) for each event. Elastic (*pP*Time factor = 1.0) *pP* delay times are used for all events other than 2017 (NK6), which has *pP*Time factor = 2.25, accounting for large delays from extensive damage in the source region. The observed amplitudes can be matched by *t** and yield values anywhere along the colored trade-off curves. Using the preferred choice of *t** and its uncertainty (0.78 ± 0.03 s; horizontal lines) from Chaves et al. (2018), based on modeling of broadband data for the 2017 event, self-consistent yield estimates and uncertainties are made for all events from the intersections with the trade-off curves. This gives the yield estimates and bounds in Table 3.

Table 3
*Yield Estimates From Teleseismic 4-Hz P Wave Initial Cycle Modeling With Ranges Based on Uncertainty Bounds in Measured Ratios and Range of t**

Event	Specified depth (m)	Yield estimate (kt)	Estimate range (kt)
2006 (NK1)	380	2.6	(1.4, 4.5)
2009 (NK2)	600	6.8	(4.4, 9.8)
2013 (NK3)	420	16.1	(8.6, 27.6)
2016a (NK4)	750	11.9	(6.9, 19.0)
2016b (NK5)	750	18.8	(12.8, 27.1)
2017 (NK6)	750	230	(180, 280)

Note. Elastic scaling factor *pP*time = 1.0 is used for all events except *pP*time = 2.25 for 2017, as preferred by Chaves et al. (2018). The range of each estimate is from consideration of the fitting over the spread of the uncertainty in *t** and the standard deviation of the event average amplitude.

measurements and the average *t** of the test site, but are restricted to the particular choice of the Mueller-Murphy model and the assumed burial depths.

The calculations in Figure 6 are all for the same elastic half-space model as used in Chaves et al. (2018), with the exception of the plot for NK6. If the true *pP* arrival is delayed relative to the elastic synthetics due to overestimation of the source *P* wave velocity (perhaps due to the presence of surficial weathering or rock layering) or by nonlinear effects due to damage around the source cavity, the amplitude contours in Figure 6 will shift and our yield estimates will change accordingly. In modeling NK6, Chaves et al. (2018) favored a *pP* arrival time delayed by a multiplicative factor, *pP*Time = 2.25, and that is used in Figure 6 for NK6. For the other events, if we increase *pP* delay time by multiplying the elastic values by *pP*Time factors of 1.5 (keeping the source depth fixed), we find that estimated yields increase by 10% to 22% for the deeper events (to 7.5 kt for NK2, 14 kt for NK4, and 22 kt for NK5) and decrease by 15% for the

shallower events (to 2.2 kt for NK1 and 13.9 kt for NK3); still giving values well within the estimated ranges in Table 3. For shallow burial depths, the elastic *pP* delay interferes destructively (Figure 5) so that a higher yield is required to match the 4-Hz data. This interference diminishes with increasing *pP* delay time, so that lower yield values match the data. Conversely, in synthetics for deeper source depths, *pP* interferes slightly constructively above 4 Hz. For increasing *pP* delay, this effect is diminished, and larger yields are required to match the data.

The sensitivity to error in the source depth used in the 4-Hz modeling is similar to that for *pP* lag variations to first order, but includes additional direct effects of source depth on the source time function. We repeat the analysis in Figure 6, using assumed source depths perturbed shallower by 100 m for NK1 (280 m), NK2 (500 m), NK3 (320 m), NK4 (650 m), and NK5 (650 m). Elastic *pP* parameters are used (*pP*Time factor = 1.0). For $t^* = 0.78$ s, the mean yield estimates are 3.0 kt (NK1), 6.7 kt (NK2), 21.5 kt (NK3), 11.1 kt (NK4), and 17.9 kt (NK5) (Figure S1). These are again well within the yield uncertainties for the preferred depth determinations in Table 3.

To evaluate the results of modeling the 4-Hz mean amplitudes, we use the yield estimates and source depths listed in Table 3 to produce synthetic *P* wave displacements, which are high-pass filtered at 4-Hz and compare the predictions with linear stacks of aligned waveforms at three arrays at varying azimuths from the source (Figure 7). Only stations with data for all events other than NK1, which has few data with acceptable signal-to-noise-ratios, are included. The amplitudes of the stacked traces are corrected for geometric spreading to 5,500 km and corresponding synthetics are compared with the data after estimating array-specific t^* values that match the average absolute amplitudes of the first-peak-to-first-trough of that array's data. This gives lower t^* for the relatively high amplitude data at Warramunga (six-station stack, $t^* = 0.54$ s) and NVAR (three-station stack, $t^* = 0.62$ s) and higher t^* for the relatively low amplitude data at Bucovina (eight-station stack, $t^* = 0.81$ s). Note that the individual path attenuation t^* vary significantly from the mean value used in modeling the event average 4-Hz amplitudes, well beyond the standard error of the mean value determined for the complete ensemble of waveforms for the event, as is expected. Each waveform comparison in Figure 7 has true relative amplitude. Overall, the source models fit the first-cycle amplitudes quite well, validating the stability of the yield estimates from the mean amplitudes. The amplitude, and likely the yield, of NK1 at Warramunga is overestimated, but the noise level is high and appears to cause some destructive interference in the data. Only the first cycle of the waveforms, indicated by the two-headed arrow, should be considered, as the half-space synthetics are not expected to specifically predict any of the later coda, which varies from array to array and between events at the same array. The strategy of the 4-Hz modeling is to avoid the need to predict the complex *pP* interference and coda behavior and to largely isolate the direct *P* energy from the source in the early part of the waveform.

4. Intercorrelation Analysis

In order to utilize more of the seismic recording than just the high-frequency content of the first 0.25 s of the *P* arrival for estimating the explosion yields, we apply a relative waveform equalization procedure to the 0.8-Hz filtered *P* wave seismograms at teleseismic and regional distances. Intercorrelation (Burger et al., 1986; Lay, 1985; Lay et al., 1984) considers two very closely located explosions recorded at multiple stations. For clarity, a brief description of the method is provided.

4.1. Intercorrelation Procedure

The observed seismograms for the *i*th isotropic explosion event observed at the *j*th station, $O_{ij}(t)$, can be expressed as the convolution of a series of filters; a source function, $S_i(t)$, a filter for all propagation effects, $G_{ij}(t)$, and the instrument response, $I_j(t)$. The observation of two events, $i = 1, 2$, at station j can thus be represented as

$$O_{1j}(t) = S_1(t)*G_{1j}(t)*I_j(t) \quad (1)$$

$$O_{2j}(t) = S_2(t)*G_{2j}(t)*I_j(t) \quad (2)$$

where * indicates convolution. The source functions for isotropic explosions are the RVPs for far-field *P* waves. The station-specific propagation effects include geometric spreading, seismic wave attenuation,

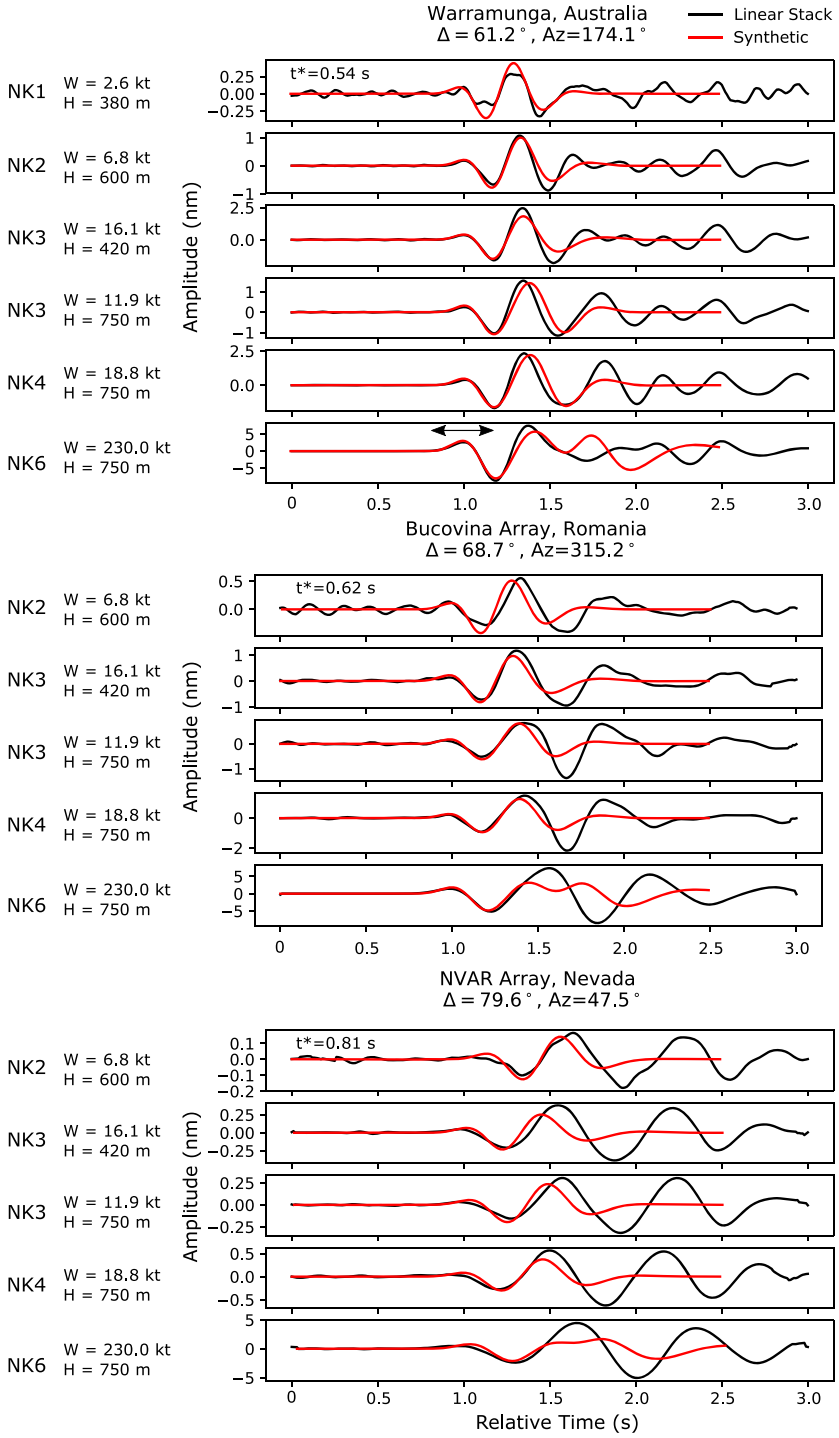

Figure 7. Comparison of observed 4-Hz filtered *P* wave signals from linear stacks of stations common to all events (black lines) at the Warramunga (six station-stack, top panel), NVAR (three-station-stack, middle panel), and Bucovina (eight-station stack, lower panel) arrays, and half-space synthetic predictions (red) for the indicated estimates of yield (W), burial depth (H), and station-specific constant t^* attenuation factor. The data and synthetics have the same filtering and each comparison has the same absolute amplitude scale. The source models are those obtained from modeling in Figure 6. The t^* for each station is tuned to match the first-peak-to-first-trough absolute amplitude. The double-headed arrow indicates the portion of the waveform that is being modeled; station-specific receiver structure and signal coda are not accounted for by the simple half-space prediction.

receiver function, and all far-field phases generated by a point-source explosion in an anelastic Earth model, as schematically shown in Figure 4. We generally do not know the details of short-period wave propagation effects that dominate the seismogram complexity at any given station, so forward modeling of the entire short-period signals has very limited predictability, even at regional distances (e.g., Rodgers et al., 2010).

Intercorrelation uses signals from nearby sources at a common station, so that all remote propagation effects, including geometric spreading, attenuation, multipathing, scattering, receiver function, and instrument response can be assumed to be identical, with only source time functions and near-source propagation effects differing between events. For an explosion in a half-space, the near-source effects involve free surface reflections *pP* and *pS*, which vary in timing if the events are at different depths. For a plane-layered near-source medium, there will be secondary differences due to multiples within the source environment, but the *pP* arrival will dominate. In the presence of rough surface topography, *pP* reflections can be complicated with focusing, defocusing, and multipathing that vary with azimuth, possibly differing even between nearby events (e.g., Avants, 2014; Rodgers et al., 2010; Stevens & O'Brien, 2018). Given that the precise location of the events beneath the 3-D topography is not known and it is an overwhelming challenge to compute teleseismic 3-D short-period propagation effects for all possible source locations within the mountainous source region, we use a flat free surface over a half-space in this study (plane layered structures were also considered, but results are not shown here as they do not differ significantly), with simple specular reflection calculations for *pP*. Thus, $G_{ij}(t)$ is parameterized as convolution of $P_{ij}(t)$, a spike-train with a *P* arrival and a *pP* arrival with relative arrival time ($\Delta t_{pP\text{-}P}$) and free surface reflection coefficient ($pP/P \sim -0.9$) computed for a given source velocity model and ray parameter for each station (ray parameters are for the IASP91 model, Kennett & Engdahl, 1991) with an operator representing all common propagation effects to the station, $R_j(t)$:

$$G_{ij}(t) = P_{ij}(t)*R_j(t) \tag{3}$$

This parameterizes the differences in the propagation terms between events to primarily correspond to the time lag between the two spikes. No matter how complex the actual far-field propagation may be, we do not need to model it, as $R_j(t)$ is common to the two traces for a given station. We define the effective source function, $S_{Eij}(t)$ to be the convolution of an estimate of the source RVP, $\widehat{S}_i(t)$, with an estimate of the station-specific propagation spike train, $\widehat{P}_{ij}(t)$:

$$S_{Eij}(t) = \widehat{S}_i(t)*\widehat{P}_{ij}(t) \tag{4}$$

The effective source functions are computed for specific trial yields and burial depths using the Mueller-Murphy model and a propagation spike train.

Ensuring that the instruments' responses are the same over time at a given station, with corrections being made if necessary, equations (1) and (2) give

$$S_{E2j}(t)*O_{1j}(t) \cong S_{E1j}(t)*O_{2j}(t) \tag{5}$$

This equation underpins the intercorrelation procedure; equivalence only holds true (the waveforms are equalized) if both events have trial effective source functions that perfectly represent the actual effective source functions (i.e., $\widehat{S}_i(t) = S_i(t)$ and $\widehat{P}_{ij}(t) = P_{ij}(t)$). Figure 8 provides examples of applying (5) to waveforms from events NK2 (2009) and NK5 (2016b) and from events NK1 (2006) and NK6 (2017), for teleseismic *P* wave signals at stations WB06 or NV01 and a regional *Pn* wave signal at station MDJ. The larger the difference in yield and burial depth, the more different the observed waveforms are (the 2006 to 2017 comparisons represent the extreme cases).

For incorrect assumed values of yield and burial depth for the two events, there will be some mismatch between the left- and right-hand sides of (5). The waveform difference residual is minimized by searching over each effective source function parameter to determine the best-fitting models. Two normalizations

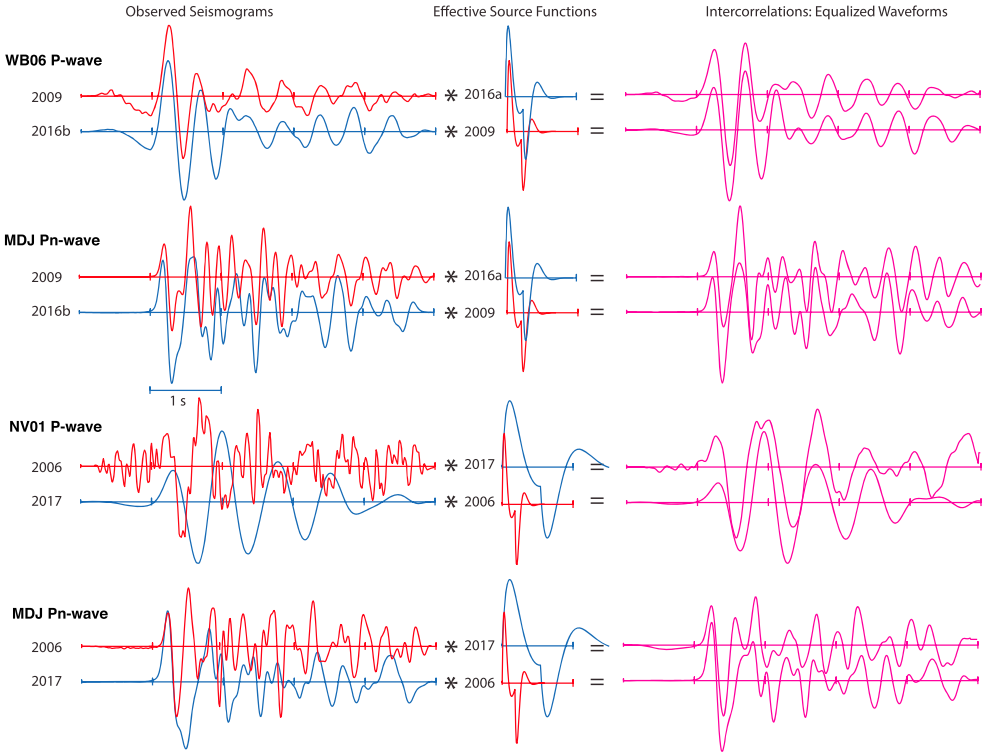

Figure 8. Examples of the intercorrelation procedure, where the observed *P* or *Pn* waves of two events (2009, NK2 and 2016b, NK5 in top two rows; 2006, NK1 and 2017, NK6 in lower two rows) at teleseismic stations WB06 (top row) or NV01 (third row) (with high-pass filter corner of 0.8 Hz) and regional station MDJ (second and fourth rows) (unfiltered) are convolved with the effective source functions (convolution of the RVP for a specific yield and burial depth with the *P* +*pP* spike train Green's function computed for each station) for the other event. This produces "intercorrelated" waveforms that will be very similar if the parameters in the effective source functions (yield and burial depth) are accurate. Searching over the effective source function parameters to optimize waveform amplitude and waveshape similarity provides optimal source parameters.

are used to appraise the waveform equalization for each trial. The first is a weighted average cross-correlation normalization given by

$$\mathrm{N_{CC}} = \frac{1}{\sum_{j=1}^{n} w_j} \sum_{\mathrm{j}}^{n} \left(\mathrm{ccc_j} \cdot w_j\right) \tag{6}$$

where n is the number of stations and ccc_j is the optimal-lag normalized cross-correlation coefficient for the jth station intercorrelation. The weighting factor, w_j is manually assigned to downweight noisy stations and upweight regional stations for which high-frequency *Pn* arrivals provide more information within the intercorrelation time window (usually 1- to 2-s long). A weighting factor of 10 is chosen for the high-sample-rate regional stations, and traces with poor signal-to-noise ratios are downweighted by as much as a factor of 0.2. Cross correlation measures the coherence of the cross-convolved waveforms and their similarity. Because both the source time functions and the observed pairs of seismograms for a given station are very similar for most events, the cross-correlation coefficient varies slowly across a substantial parameter space. Appraisal of best-fitting models based only on cross correlation is also biased toward alignment of high-amplitude pulses. To mitigate this, we also use a second parameter to evaluate the model parameters.

This second parameter retains the absolute amplitude information. The amplitude error is

$$ERR_{\mathrm{amp}} = w_j \sum_{j=1}^{n} \sum_t \left[\theta_{1\mathrm{j}}(t) - \theta_{2j}(t)\right]^2 \cdot \frac{1}{F_{\mathrm{scale}} \sqrt{\sum_t S_{E1j}(t)^2 \cdot \sum_t S_{E2j}(t)^2}} \tag{7}$$

where $\theta_{1\mathrm{j}}(t)$ and $\theta_{2\mathrm{j}}(t)$ are the left and right sides of (5), respectively, for the jth station intercorrelation. The squared difference of the cross convolutions, $[\theta_{1\mathrm{j}}(t) - \theta_{2\mathrm{j}}(t)]^2$, is normalized by the power of the effective

source functions and by F_{scale}, a factor used to balance the amplitude error. The waveform error is computed for each station for a specified time range and then summed over the total number of stations, n. The logarithm of the ERR_{amp} is then averaged by the sum of station weights:

$$N_{ERR} = \frac{\log_{10}(ERR_{amp})}{\sum_{j=1}^{n} w_j} \tag{8}$$

and the final amplitude norm is taken to be

$$N_{AMP} = 10^{N_{ERR}} \tag{9}$$

Normalizing by the power in the effective source functions reduces, but does not eliminate, the effect of amplitude scaling of the effective source functions with increasing yield, which increases the power in $\theta_{1j}(t)$ and $\theta_{2j}(t)$ and, in turn, the squared difference between them.

This method can be applied to estimate yields with no independent constraints, but the technique is intrinsically mostly sensitive to relative differences in source depth and yield, rather than absolute values. Thus, a suite of yields and depth of burials for both events can suitably reduce the residual between both sides of (5). The differential sensitivity somewhat reduces influence of error in the seismic velocity structure used to calculate *pP* delay times and amplitudes, with regional phases being more sensitive due to their larger ray parameters. We again use a source *P* wave velocity of 5.5 km/s, as this is the standard value for the Mueller-Murphy granite source model (e.g., Stevens & Day, 1985). If we lower the near-surface velocity in layered models to allow for weathering, we find that relative yields and relative depths can vary by several percent, which is small compared to overall uncertainties.

4.2. Intercorrelation Results

Relatively large data sets are used to enhance the sensitivity of collective waveform equalization for each event pair; for example, there are 166 waveform pairs for NK5 and NK6; 190 for NK5 and NK4; 162 for NK5 and NK3; 110 for NK5 and NK2, and 22 for NK5 and NK1. Figure 9 shows the full data set for the NK5 and NK2 comparison, comprised of 108 *P* wave seismogram pairs, mostly from high-frequency array channels, along with two regional *Pn* seismogram pairs. The latter have the highest signal-to-noise ratios and broadest band energy. Many of the additional data are shown as event pairs in Figures S2 and S3. Each event can be intercorrelated with all other events, giving multiple measures of relative yields and source depths.

We considered wide ranges of candidate yields and depths for each event, determining the preferred parameters for the other five events in each case, confirming that absolute yield and depth determinations are not well resolved, but relative yield measures are reasonably stable. Absolute depth resolution is similarly limited, and there are systematic trade-offs between relative yield and relative depth estimates. As in previous applications of intercorrelation, independent specification of any single event yield and depth (which were openly known for some U.S. tests at the Nevada and Amchita test sites) allows absolute yield and depth estimates to be made for all other events. As a preliminary reference, we adopt the yield estimate (18.8 kt) for a source depth of 750 m for event 2016b (NK5) obtained from the 4-Hz modeling described above. Recall that perturbing the source depth by −100 m only slightly changed the yield estimate to 17.9 kt, so this is a stable reference case. While this estimate is linked to the t^* value that Chaves et al. (2018) directly estimated from modeling the 2017 (NK6) event, the waveforms for NK6 differ significantly from all other events, so it is less reliable as a reference event for the full waveform modeling.

For the reference model for NK5, we search over broad ranges of yield and burial depth for each of the other five events, finding results summarized in column 2 (green) of Table S2, using the norms in (6) and (7) to define preferred values for the 1-s time interval from 0.1 s before the first arrival to 0.9 s after. The results are listed for elastic *pP* parameters (*pP*Time factor = 1.0) for all events, but for NK6 results are also shown for the delayed *pP* (*pP*Time factor = 2.25) inferred by Chaves et al. (2018). The intercorrelated waveforms for NK5 (yield 18.8 kt, H= 750 m) and NK2 (yield 5.1 kt, H = 730 m) are shown in Figure 10 to illustrate the waveform equalization. The convolutions with the estimate effective source functions slightly modify the waveshapes relative to the raw data in Figure 9, but the relative amplitudes are much more similar

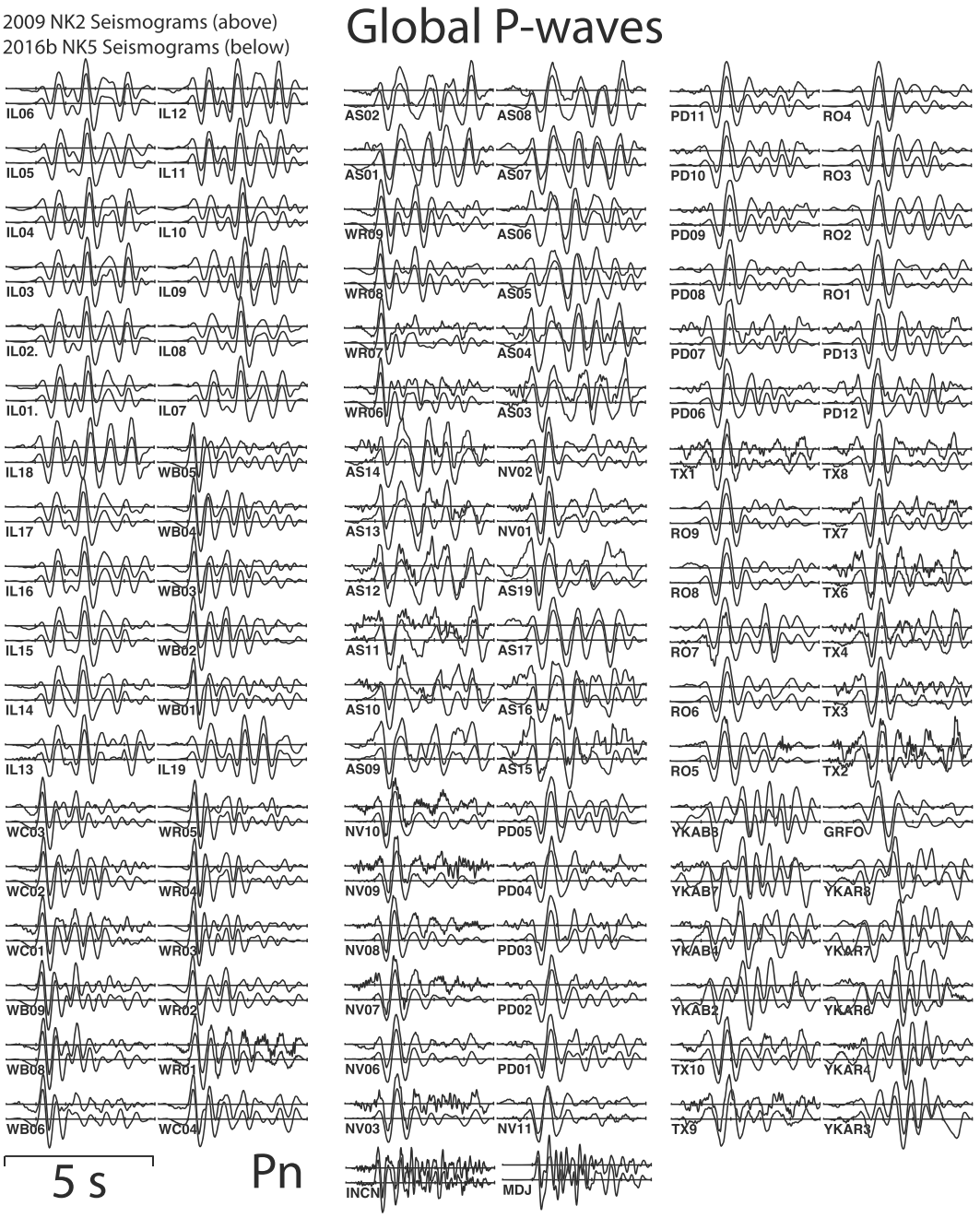

Figure 9. Seismogram pairs for 108 teleseismic *P* and two regional *Pn* observations for the 2009 (NK2) and 2016b (NK5) events. The *P* wave data are high-pass filtered with a corner at 0.8 Hz; MDJ is unfiltered, while INCN is high-pass filtered with corner at 1 Hz. The amplitudes of all traces are normalized to the peak amplitude in the 5-s windows.

due to the equalization. Figure 11 shows the trade-off curves for the amplitude norm (7) over ranges of yield and depth estimates for the five events. The amplitude misfit surfaces display complex trade-offs between yield and depth, sometimes with better resolution of yield (NK2), sometimes with better resolution of depth (NK3), and sometimes with direct trade-off (NK4). Using the parameters estimated for each event relative to the reference case for NK5, each event was in turn used as a reference event (yellow highlights in Table S2), giving the results in other columns in Table S2. Recognizing that the intercorrelation procedure is primarily sensitive to relative parameters, Table 4 normalizes all of the columns in Table S2 by the corresponding yield estimates for NK5, along with giving average yield ratios relative to NK5. This

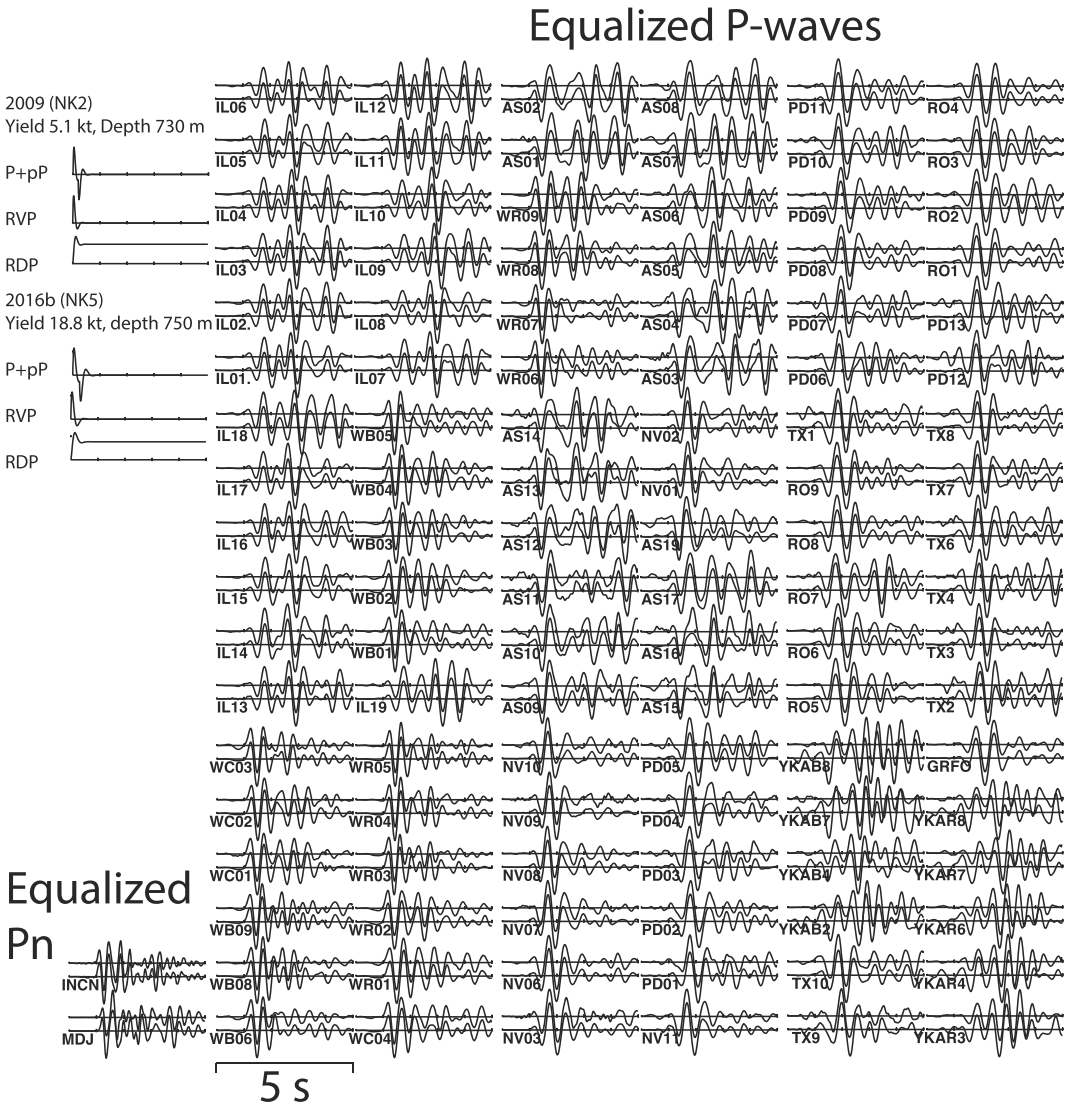

Figure 10. The equalized waveforms for the data in Figure 9 where the effective source models for 2009 (NK2) and 2016b (NK5) are shown at the upper left (labeled *P+pP*), along with the corresponding reduced velocity potential and reduced displacement potential. The NK2 observation convolved with the NK5 effective source model is the upper trace in each pair, while the NK5 observation convolved with the NK2 effective source model is the lower trace in each pair. The yield and depth for NK5 were specified and a search over yield and depth for NK2 minimized the amplitude misfit norm for the indicated yield and depth (see Figure 11).

highlights the significant precision of the relative size estimates in this case. While there is up to 30% variability in yield estimates from the various reference event combinations, there is greater variation in depth for these unconstrained searches, which directly contributes to the variation in yield estimates.

Given that the reference yield estimate for NK5 has uncertainty, we explore the effect of varying that value. Table S3 shows results found if the initial reference yield for NK5 is assumed to be 12.5 kt for 750-m source depth. The unconstrained search over yield and depth of burial gives average yield ratios summarized in Table 5, which are within 15% of those in Table 4. The yield ratio results in Tables 4 and 5 exhibit scatter from fluctuation in estimated depth, particularly for NK2, NK3, and NK6. This is associated with there being two or more local minima in the waveform misfit surfaces. If the local minimum at larger depth is slightly more pronounced, a larger yield is estimated. The limitations of the data sets and model parameterization are responsible for this instability. The averaging of multiple combinations of intercorrelations does tend to give yield ratio estimates that are quite consistent and independent of the initial reference event yield.

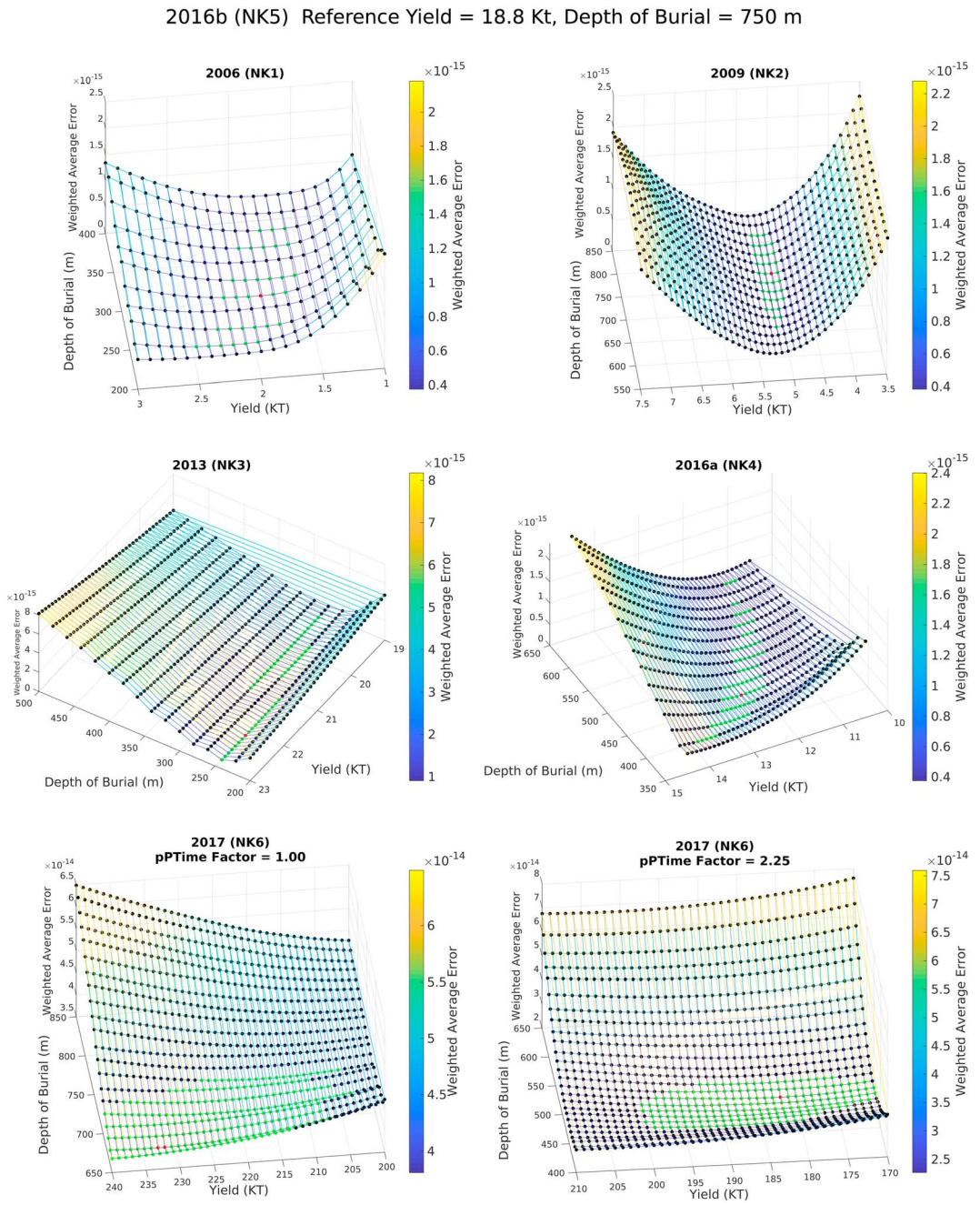

Figure 11. Intercorrelation search over yield and burial depth for each of the nuclear tests relative to the 2016b (NK5) event, which has fixed yield estimate of 18.8 kt and depth of burial of 750 m, as used in the 4-Hz modeling. The weighted waveform amplitude misfit norm is shown for each estimate of the parameters of the effective source function for the indicated events, with red dots indicating the minimum misfit, green dots indicating parameters giving up to 10% increase in misfit norm, used to specify bounds on yield and depth estimates. The surfaces are color scaled by misfit outside the green dot regions. Elastic *pP* delay times (*pP*Time factor = 1.0) are used for all events except for the 2017 (NK6) event, for which *pP*Time factor = 2.25 is used, giving delayed *pP* arrivals, as indicated in the modeling by Chaves et al. (2018).

The elastic half-space calculations involve a rather high source region velocity and short *pP* delay times, and it is likely that actual elastic structure is slower, as discussed above. We thus also perform unconstrained intercorrelations of all event combinations using *pP*Time factors of 1.25, 1.50, 1.75, and 2.0. Estimates of the yield and source depth for NK4 for models of NK5 with a yield of 18.8 kt and 750-m burial depth, with different *pP*Time combinations are shown in Table S4. Based on the location of these two events (Figure 1), similar depths are expected, and very consistent yield and depth estimates are found when *pP*Time is the

Table 4
Yield Ratios From Unconstrained Intercorrelation Searches Relative to a Starting Reference of 2016b (NK5) With Yield of 18.8 kt and Depth of Burial of 750 m

Event	2017	2016b	2016a	2013	2009	2006	Average
2017 *pP*Time 1.0 (NK6)	11.3 660 m REF	12.3 660 m	14.8 520 m	11.5 1,350 m	15.8 520 m	10.9 1,380 m	13
2017 *pP*Time 2.25		9.7 500 m	8.5 480 m	9.6 520 m	10.2 400 m	10.0 580 m	9.6
2016b (NK5)	1.0 560 m	1.0 750 m START	1.0 440 m	1.0 840 m	1.0 780 m	1.0 940 m	1.0
2016 (NK4)	0.60 500 m	0.67 430 m	0.57 430 m REF	0.73 329 m	0.66 460 m	0.51 840 m	0.62
2013 (NK3)	0.72 500 m	1.19 240 m	0.95 260 m	1.19 240 m REF	0.70 800 m	0.85 300 m	0.93
2009 (NK2)	0.35 340 m	0.27 730 m	0.23 580 m	0.28 740	0.27 730 m REF	0.25 320 m	0.28
2006 (NK1)	0.12 280 m	0.10 280 m	0.10 280 m	0.09 280	0.11 220 m	0.09 280 m REF	0.10

Note. Each column represents a search of yields and depths relative to the event labeled at the top of the column, with the yields normalized by the estimate found for 2016b (NK5). The absolute values of the yields and uncertainty ranges are shown in Table S2 in the supporting information. Elastic *pP*Time factor = 1.0 was assumed for all cases, with an additional solution for 2017 for *pP*Time factor = 2.25. The average values of the yield ratios and source depth estimates for the six suites of estimates are shown on the right.

same for both events with values of 1.25 to 2.0. Using a larger *pP*Time factor for NK4 than for NK5 leads to unlikely shallow depth estimates, while using a lower *pP*Time factor for NK4 than for NK5 leads to unlikely deep depth estimate. It appears most reasonable to use uniform *pP*Time factors. A subset of results for all events using a reference yield of 18.8 kt for NK5 and uniform *pP*Time factors from 1.0 to 1.5 is listed in Table S5. As *pP*Time increases, there are moderate increases and decreases in estimated yields, with the largest fluctuations found when depth changes significantly. If the NK5 reference event depth is changed to 625 m, the estimated depths tend to shallow slightly, and there is somewhat less variation in yield and depth estimates (Table S6). Searching over all possible depths and *pP* delay parameters for all events is not particularly useful, given the complex topology of the waveform misfit curves. So, our strategy for obtaining preferred yield estimates is to impose a priori constraints on the depths.

We estimate the burial depth of each event based on the topographic relief from the tunnel adits to positions below the epicentral location estimates of Myers et al. (2018). We project the centers of the location ellipses in Figure 1 to depth, assuming, in the first case, horizontal tunneling, and in the second case, tunneling with a 4% grade. These depth estimates are given in Table 6. Given the variable topography, the horizontal tunnel assumptions provide reasonable maximum overburden estimates, while 4% grade not only allows for drainage but also may partially account for minimum depth to the surface being less than vertical depth.

Fixing these two sets of depth estimates, we compute relative yields using intercorrelation varying only yield and uniform *pP*Time factor from 1.0 to 1.5, again initiating cross combinations with NK5 having a yield of 18.8 kt. Time windows 2.1-s long are used for computing the waveform norms for the depth-constrained intercorrelations. Results for the depths predicted by horizontal tunneling are shown in Table S7 for *pP*Time factor = 1.0 and in Table S8 for *pP*Time factor = 1.5. Results for the depths predicted by tunneling with a 4% grade are shown in Table S9 for *pP*Time factor = 1.0 and in Table S10 for *pP*Time factor = 1.5. Constraining burial depths suppresses variation of estimated yield for NK1–NK5 significantly in Tables

Table 5
Yield Ratios From Unconstrained Intercorrelation Searches Relative to a Starting Reference of 2016b (NK5) With Yield of 12.5 kt and Depth of Burial of 750 m

Event	2017	2016b	2016a	2013	2009	2006	Average
2017 *pP*Time 1.0 (NK6)	14.1 460 m REF	15.6 460 m	20.0 400 m	14.9 480 m	18.0 400 m	19.9+ 320 m	14
2017 *pP*Time 2.25		8.5 460 m	12.4 280 m	8.3 520 m	9.8 320 m	11.9 600 m	10
2016b(NK5) *pP*Time 1.0	1.0 500 m	1.0 750 m START	1.0 700 m	1.0 780 m	1.0 820 m	1.0 940 m	1.0
2016a (NK4)	0.61 480 m	0.68 400 m	0.68 400 m REF	0.79 300 m	0.59 760 m	0.54 800 m	0.65
2013 (NK3)	0.73 440 m	1.22 220 m	1.22 220 m	1.23 220 m REF	1.06 240 m	0.68 940 m	1.02
2009 (NK2)	0.31 380 m	0.27 680 m	0.32 320 m	0.48 180 m	0.27 680 m REF	0.24 320 m	0.32
2006 (NK1)	0.12 280 m	0.10 280 m	0.12 280 m	0.10 220 m	0.11 220 m	0.09 280 m REF	0.11

Note. Each column represents a search of yields and depths relative to the event labeled at the top of the column, with the yields normalized by the estimate found for 2016b (NK5). The absolute values of the yields and uncertainty ranges are shown in Table S3 in the supporting information. Elastic *pP*Time factor = 1.0 was assumed for all cases, with an additional solution for 2017 for *pP*Time factor = 2.25. The average values of the yield ratios and source depth estimates for the six suites of estimates are shown on the right.

S7–S10 compared to the unconstrained intercorrelation estimates in Tables S2 and S3. For example, assuming a 4% tunnel grade and *pP*Time factor = 1.0 (Table S9) results in <11% ranges in the yield estimates for NK1, NK2, NK3, NK4, and NK5. Differences relative to assuming horizontal tunneling depths are comparable. NK6 has larger variations, mainly due to the longer period duration of the RDP and more complex *pP* interference behavior. Comparing the cases of *pP*Time factor = 1.0 to *pP*Time factor = 1.5 for the two sets of burial depths (Tables S7 vs. S8 and Tables S9 vs. S10), indicates small effect on estimated yields of NK4 and NK5 (1–2% difference) and larger effect on NK1 (42% difference) and NK3 (30% difference). For NK1 and NK3, yield estimates decrease when increasing the *pP*Time factor to 1.5, whereas they slightly increase for decreasing depth of burial.

Table 6
Estimated Vertical Burial Depths Assuming Epicentral Locations Shown in Figure 1 (Table 1), a Digital Elevation Map From Shuttle Radar Topography Mission (SRTM) Data, Estimated Tunnel Adit Locations, and Either Horizontal Tunneling (Middle Column) or Tunneling With a 4% Grade (Right Column)

Event	No grade	4% grade
2006 (NK1)	500 m	430 m
2009 (NK2)	670 m	600 m
2013 (NK3)	480 m	430 m
2016a (NK4)	790 m	710 m
2016b (NK5)	790 m	710 m
2017 (NK6)	790 m	710 m

The yield estimates determined by intercorrelations using the NK5 reference yield of 18.8 kt for *pP*Time factors of 1.0, 1.25, and 1.5 are shown in Table 7. Our preferred yield estimates allow for both a tunnel grade of 4% and a delay of *pP* by a factor of 1.25 for the five smaller events and larger *pP* delay by a factor of 2.25 for the 2017 event. The yield estimates are 1.4 kt (NK1), 5.0 kt (NK2), 13.2 kt (NK3), 11.2 kt (NK4), 18.8 kt, (NK5), and 215–250 kt (NK6). All of these are tied to the baseline yield assumed for NK5. The velocity structure is not known in detail, and some *pP* delay relative to a uniform half-space is to be expected for all events, and we view *pP*Time factor = 1.25 as a reasonable first-order adjustment for velocity structure error. For 2017, the much greater damage zone around the large explosion will impact more of the *pP* surface reflection than for the smaller events, augmenting the *pP* perturbation (Figure 12). Thus, some preference is given for the 250-kt estimate of yield which is for

Table 7
Yields and their Uncertainty Bounds Estimated by Intercorrelation Relative to Reference Values for 2016b (NK5), of Yield = 18.8 kt, and Depth of Burial = 750 m

Event	*pP*Time 1.0 Horizontal	*pP*Time 1.25 Horizontal	*pP*Time 1.5 Horizontal	*pP*Time 1.0 4% grade	*pP*Time 1.25 4% grade	*pP*Time 1.5 4% grade
2017 *pP*Time Factor 2.25	250 kt (205–330 kt) 790 m	285 kt (225-365 kt) 790 m	290 kt (240-370 kt) 790 m	215 kt (180-260 kt) 710 m	**250 kt (215-300 kt) 710 m**	265 kt (230-320 kt) 710 m
2017 (NK6)	200 kt (180–225 kt) 790 m	205 kt (185–225 kt) 790 m	210 kt (195–225 kt) 790 m	215 kt (195–240 kt) 710 m	215 kt (200–240 kt) 710 m	220 kt (205–240 kt) 710 m
2016b (NK5)	18.8 kt 790 m REF	18.8 kt 790 m REF	18.8 kt 790 m REF	18.8 kt 710 m REF	**18.8 kt 710 m REF**	18.8 kt 710 m REF
2016a (NK4)	11.3 kt (10.7–11.9 kt) 790 m	11.2 kt (10.6–11.8 kt) 790 m	11.0 kt (10.4–11.7 kt) 790 m	11.3 kt (10.8–11.9 kt) 710 m	**11.2 kt (10.6–11.8 kt) 710 m**	11.1 kt (10.5–11.7 kt) 710 m
2013 (NK3)	13.8 kt (12.6–15.3 kt) 480 m	12.2 kt (11.0–13.6 kt) 480 m	10.1 kt (8.5–11.9 kt) 480 m	14.4 kt (13.2–15.2 kt) 430 m	**13.2 kt (11.9–14.7 kt) 430 m**	11.7 kt (10.7–13.3 kt) 430 m
2009 (NK2)	5.1 kt (4.8–5.4 kt) 670 m	4.8 kt (4.5–5.1 kt) 670 m	4.4 kt (3.9–4.9 kt) 670 m	5.2 kt (4.9–5.5 kt) 600 m	**5.0 kt (4.7–5.3 kt) 600 m**	4.7 kt (4.4–5.0 kt) 600 m
2006 (NK1)	1.6 kt (1.4–1.9 kt) 500 m	1.2 kt (1.1–1.5 kt) 500 m	0.9 kt (0.8–1.1 kt) 500 m	1.8 kt (1.5–2.0 kt) 430 m	**1.4 kt (1.2–1.6 kt) 430 m**	1.1 kt (1.0–1.3 kt) 430 m

Note. Depths are constrained to the two sets of values in Table 6. Results for all cross combinations for each choice of burial depth and *pP*Time factor are given in Tables S7–S10 in the supporting information. The overall preferred values are highlighted in bold in column 5, which is for *pP*Time factor = 1.25 and depths for assumed 4% tunnel grade.

*pP*Time factor = 2.25, as used by Chaves et al. (2018). The uncertainty estimates are case specific and do not capture all model uncertainty by any means. The explosion model and its scaling, the specific source depths, the elastic wave propagation, the use of a flat free surface, all involve assumptions that affect these estimates. However, within the model space considered, the results are generally stable with the largest variation being for the poorly recorded 2006 (NK1) event.

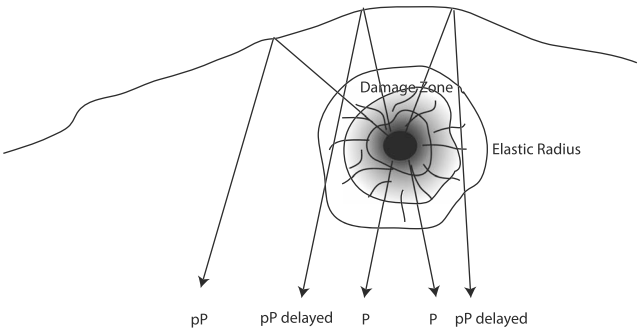

Figure 12. Schematic of how the surface reflections, *pP*, may be selectively affected by the damage zone around the explosion cavity. Larger explosions, with larger damage zone radii will affect a wider range of *pP* paths, with the 2017 (NK6) event expected to have much stronger and more extensive nonelastic effects on *pP* than the smaller events.

5. Spectral Ratio Tests

Acknowledging the nonuniqueness of the preferred models, it is useful to verify that they are reasonable. We evaluate the results of the waveform equalization by comparing spectral ratios of high quality regional *Pn* data and source functions for our preferred yield and depth estimates. For two closely located isotropic explosions, computing the spectral ratio cancels the propagation effects from the source region to a common receiver, isolating the ratio of the effective source functions. The regional seismograms from station MDJ (with instruments equalized to 2017 response) allow us to recover broadband spectra from about 0.5 to 10 Hz for windowed *Pn* arrivals. For the synthetics, we compute the RVP effective source function (*Pn* + *pPn*) using the preferred yield and depth of burial estimates from intercorrelation with 4% tunneling grade and *pP*Time factor =1.25 (Table 7, column 5). For NK6 we use the result for *pP*Time factor = 2.25. The data and model spectra and spectral ratios of NK6 to every other event are shown in Figure 13.

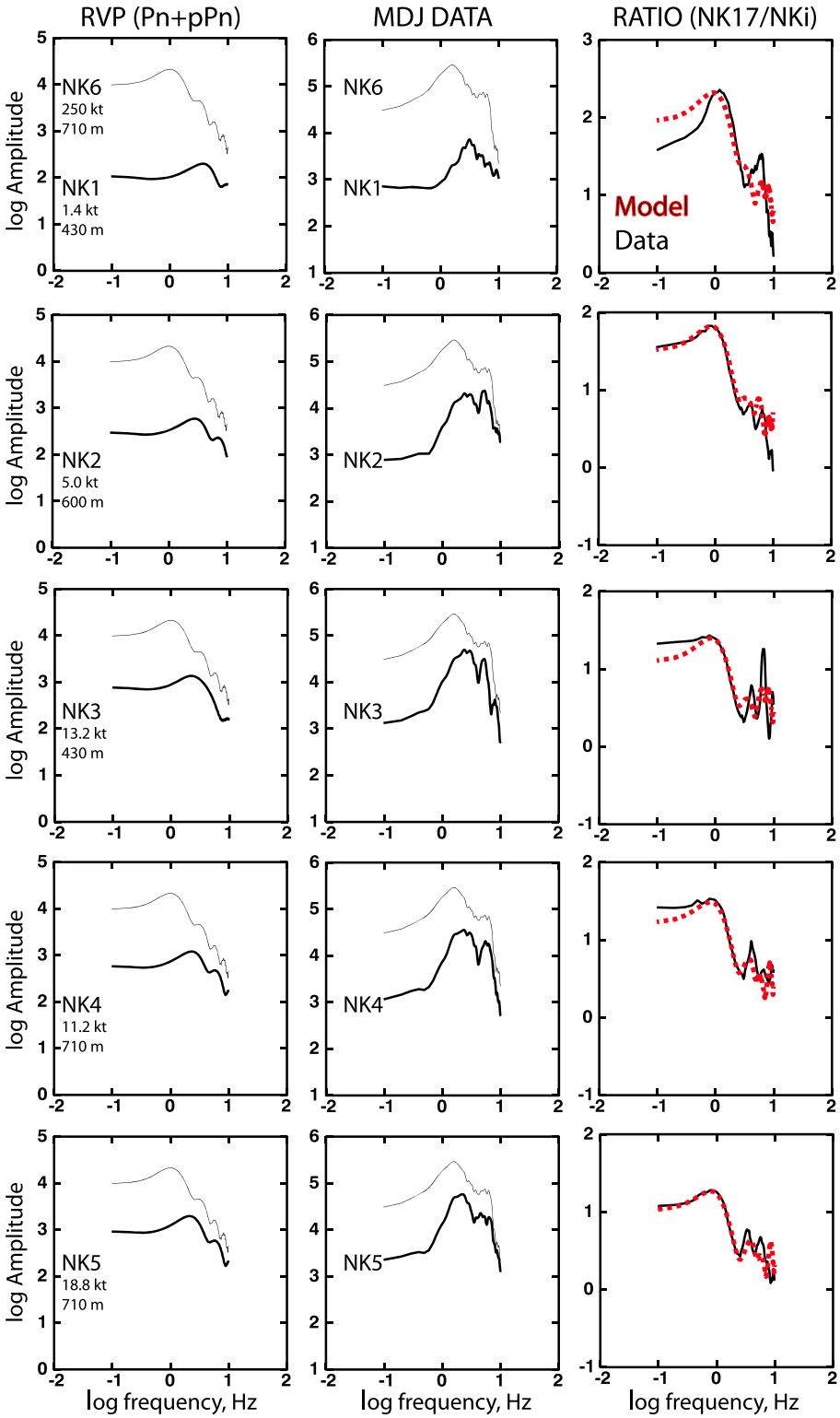

Figure 13. Comparison of effective source function spectra for the six nuclear explosions using the preferred intercorrelation values in Table 7 (left column) with observed *Pn* spectra for regional station MDJ, (middle column), with spectral ratios shown on the right (intercorrelation results are in dashed red lines, data in black).

Table 8
*Yield Estimates From Teleseismic 4-Hz P Wave Initial Cycle Modeling With Ranges Based on Uncertainty Bounds in Measured Ratios and Range of t**

Event	Specified depth (m)	Yield estimate (kt)	Estimate range (kt)
2006 (NK1)	430	2.3	(1.3, 3.8)
2009 (NK2)	600	5.5	(4.5, 6.6)
2013 (NK3)	430	14.3	(8.0, 23.9)
2016a (NK4)	710	12.5	(7.5, 19.2)
2016b (NK5)	710	19.7	(13.4, 28.2)
2017 (NK6)	710	221	(148, 328)

Note. Elastic scaling factor *pP*time = 1.25 is used for all events except *pP*time = 2.25 for 2017, as preferred by Chaves et al. (2018), and depths are for 4% grade tunneling.

The model spectral ratios match the data very well in the 0.5- to 5-Hz passband. As can be seen in the individual data spectra there is very little signal below 0.5 Hz other than for NK6, so the long-period level is not expected to be fit well. Nonetheless, in the 0.5- to 2-Hz band there is clearly a bump in the spectral ratios that is matched well by the overshoot of the Mueller-Murphy source model. This would not be well matched by source models that lack overshoot. The critical passband for this comparison is from 1 to 5 Hz, and the models perform well in this band, even for the 250- to 1.4-kt comparison of NK6 and NK1. While the absolute yield levels are not resolved by these ratios, the relative yield estimates from intercorrelation are well supported by this analysis.

As a test of consistency between the intercorrelation results and the 4-Hz amplitude modeling, we use the preferred burial depths and *pP*Time factors (Table 7, column 5) in again forward modeling of the 4-Hz amplitudes. This gives the yield estimates listed in Table 8. These can be compared with the results in Table 3, based on slightly different depth and *pP*Time factors. The *t** parameter is held fixed in this modeling at 0.78 ± 0.03 s. Only slight differences in estimated yield result from the newly specified burial depths and *pP*Time factors, indicating general compatibility of the different analyses, well within the inferred bounds of the estimates. We expect that the intercorrelation procedure provides a better yield estimate for the 2006 event because it uses broader bandwidth, whereas the 4-Hz amplitude may be affected by *pP* for this shallow, low signal-to-noise ratio event.

6. Discussion and Conclusions

Direct calibration of magnitude-yield relationships for a given nuclear test site is required for very high confidence seismic yield estimation, but that is not available for the North Korean test site. The yield estimates obtained in this study from both the 4-Hz modeling and intercorrelation can be used to predict magnitude-yield scaling curves. Figure 14 shows simple linear regressions of the 4-Hz yield estimates (Table 3) and the preferred intercorrelation estimates (Table 7, column 5) on NEIC m_b values, m_{bNEIC}. The two sets of yield estimates are generally similar, with NK1 having the largest deviation, and likely being less reliable for the 4-Hz estimation due to data limitations. The yield-scaling slope for the 4-Hz estimates is about 1.0, while it is 0.9 for the intercorrelation results; both of these are significantly higher than yield-scaling slopes for

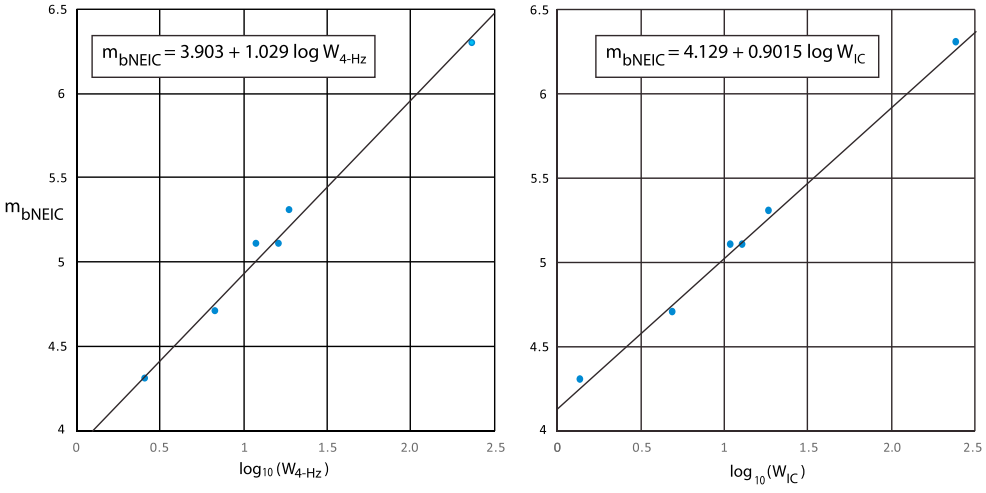

Figure 14. Empirical m_b-yield relationships for the six North Korean underground nuclear explosions between m_{bNEIC} and (a) yields ($W_{4\text{-Hz}}$) estimated from modeling of the 4-Hz filtered teleseismic *P* waves data using $t^* = 0.78$ s in Figure 6, and (b) yields (W_{IC}) estimated from preferred intercorrelations with constrained depths listed in Table 7, column 5. Simple linear regressions give the intercept and slopes of each relationship.

m_{bNEIC} estimated for Semipalatinsk (0.75) and NTS (0.81; Murphy et al., 2013). This indicates that one cannot transfer magnitude-yield relationships from either of those sites to North Korea. It should be kept in mind that the NEIC magnitudes in Figure 14 have very large variation in data sampling, so the significance of the specific slope and intercept values are difficult to evaluate. The intercorrelation and location constraints on depths indicate that the North Korean tests include a wide range of scaled burial depths, with the yields of smaller events being higher for a given magnitude than for normally buried events typically used in magnitude-yield calibration relationships. That would tend to increase the yield-scaling slopes relative to other sites. The relatively high slopes found here are also consistent with the relatively large t* estimated for this test site, as this reduces high-frequency content of all events. The magnitude-yield relationship for the intercorrelation yield estimates, $W_{IC,}$ is our preferred "empirically" calibrated model.

As emphasized throughout this paper, remote seismological estimation of explosion yields without direct calibration is fraught with many assumptions that undermine uniqueness. Our simple elastic half-space calculations do not account for complex near-source 3-D wave propagation effects, particularly for depth phases. In addition, the *pP* depth phase may be delayed and possibly reduced in amplitude for some seismic stations due to propagation downward through the damage zone of each explosion (Figure 12). While the much larger yield of NK6 makes it likely that this effect is significantly greater for this event relative to the smaller events, fully nonlinear hydrodynamic calculations are required to further evaluate such effects.

The modeling of 4-Hz high-pass filtered *P* waveforms is intended to suppress effects of *pP* and path structure, but this depends on source depth, path attenuation, and influence of the minor long-period energy allowed into the signal by the filter. Intercorrelation provides a broader band estimation of relative yield without needing to specify the remote propagation effects, but requires explicit representation of the free surface interaction. We do not account for variations in *pP* amplitude and azimuthal delay variations that will result from surface topography. Numerical models to do so are being pursued, but initial work (Avants, 2014) indicates modest fluctuations in *pP* amplitudes for computations with realistic surface topography. The true 3-D source structure and device emplacement locations are unknown, contributing uncertainty to the intercorrelation results. The absolute depths of NK1, NK2, and NK3 are particularly uncertain, as small lateral variations in epicentral location could result in large changes in burial depth beneath the steep slopes of Mount Mantap. If NK4, NK5, and NK6 are correctly located beneath the summit, there is less uncertainty in these depth estimates, but the true tunnel geometry is not known. The specification of 18.8 kt as the reference yield of NK5 for intercorrelation is based on the 4-Hz modeling, and this value is tied to the *t** estimate of Chaves et al. (2018).

All of the results given here are specific for the Mueller-Murphy source model (Mueller & Murphy, 1971), and do not capture associated source model parameterization uncertainty. Several other nuclear explosion models have been proposed, including Haskell (1967), von Seggern and Blandford (1972), Helmberger and Hadley (1981), Denny and Johnson (1991), and Walter and Ford (2018). These have different spectral shape and different depth and yield-scaling attributes, and some concerns have been raised about the Mueller-Murphy model (e.g., Patton & Pabian, 2014; Walter & Ford, 2018). However, the Mueller-Murphy model remains the most comprehensively parameterized model, and as shown in the modeling here, it is very effective at representing the seismic data for reasonable parameters. If future work validates a different preferred nuclear explosion source model with yield and depth scaling for variable source media, similar modeling and intercorrelation analysis may improve the yield estimates for the North Korean test site. Use of a different source spectral shape will likely require use of different attenuation operators, which may need to be frequency dependent (e.g., Burger et al., 1987).

Acknowledgments
All data used in this study were accessed from the openly available archive at the Data Management Service of the Incorporated Research Institutions for Seismology (https://www.iris.edu/hq/). We thank C. Saikia for providing his software for computing the Mueller-Murphy time domain response and for an advance copy of his paper describing the derivation. R. Blandford encouraged analysis of the 4-Hz first cycle amplitudes to minimized influence of *pP*. Steve Gibbons and Sean Ford provided helpful reviews of the manuscript. This paper is supported by the Air Force Research Laboratory under contract FA9453-18-C-0065.

References

Alvizuri, C., & Tape, C. (2018). Full moment tensor analysis of nuclear explosions in North Korea. *Seismological Research Letters*, *89*(6), 2139–2151. https://doi.org/10.1785/0220180158

Assink, J. D., Averbuch, G., Smets, P. S. M., & Evers, L. G. (2016). On the infrasound detected from the 2013 and 2016 DPRK's underground nuclear tests. *Geophysical Research Letters*, *43*, 3526–3533. https://doi.org/10.1002/2016GL068497

Avants, M. (2014). Effects of near-source heterogeneity on wave fields emanating from crustal sources observed at regional and teleseismic distances. Ph.D. Thesis, University of California, Santa Cruz, 135 pp.

Barth, A. (2014). Significant release of shear energy of the North Korean nuclear test on February 12, 2013. *Journal of Seismology*, *18*, 605–615. https://doi.org/10.1007/s10950-014-9431-6

Burger, R. W., Burdick, L. J., & Lay, T. (1986). Estimating the relative yields of Novaya Zemlya tests by waveform intercorrelation. *Geophysical Journal of the Royal Astronomical Society*, *87*, 775–800.

Burger, R. W., Lay, T., & Burdick, L. J. (1987). Average Q and yield estimates from the Pahute Mesa test site. *Bulletin of the Seismological Society of America*, *77*, 1274–1294.

Carluccio, R., Giuntini, A., Materni, V., Chiappini, S., Bignami, C., D'Ajello Caracciolo, F., et al. (2014). A multidisciplinary study of the DPRK nuclear tests. *Pure and Applied Geophysics*, *171*(3), 341–359. https://doi.org/10.1007/s00024-012-0628-8

Cesca, S., Heimann, S., Kriegerowski, M., Saul, J., & Dahm, T. (2017). Moment tensor inversion for nuclear explosions: What can we learn from the 6 January and 9 September 2016 nuclear tests, North Korea? *Seismological Research Letters*, *88*(2A), 300–310. https://doi.org/10.1785/0220160139

Chaves, E., Lay, T., & Voytan, D. P. (2018). Yield estimate (230 kt) for a Mueller-Murphy model of the 3 September 2017, North Korean nuclear test ($m_{bNEIC} = 6.3$) from teleseismic broadband *P* waves assuming extensive near-source damage. *Geophysical Research Letters*, *45*, 10,314–10,322. https://doi.org/10.1029/2018GL079343

Chiang, A., Ichinose, G. A., Dreger, D. S., Ford, S. R., Matzel, E. M., Myers, S. C., & Walter, W. R. (2018). Moment tensor source-type analysis for the Democratic People's Republic of Korea—Declared nuclear explosions (2006–2017) and 3 September 2017 collapse event. *Seismological Research Letters*, *89*(6), 2152–2165. https://doi.org/10.1785/0220180130

Chun, K.-Y., Wu, Y., & Henderson, G. A. (2011). Magnitude estimation and source discrimination: A close look at the 2006 and 2009 North Korean underground nuclear explosions. *Bulletin of the Seismological Society of America*, *101*(3), 1315–1329. https://doi.org/10.1785/0120100202

Coblentz, D., & Pabian, F. (2015). Revised geologic site characterization of the North Korean test site at Punggye-Ri. *Science and Global Security*, *23*(2), 101–120. https://doi.org/10.1080/08929882.2015.1039343

Denny, M. D., & Johnson, L. R. (1991). The explosion seismic source function: Models and scaling laws reviewed. In *Explosion Source Phenomenology*, *Geophysical Monograph* (Vol. 65, pp. 1–24). Washington DC: American Geophysical Union.

Ford, S. R., Dreger, D. S., & Walter, W. R. (2009). Source analysis of the Memorial Day explosion, Kimchaek, North Korea. *Geophysical Research Letters*, *36*, L21304. https://doi.org/10.1029/2009GL040003

Futterman, W. I. (1962). Dispersive body waves. *Journal of Geophysical Research*, *67*, 5279–5291.

Gibbons, S. J., Kvaerna, T., Näsholm, S. P., & Mykkeltveit, S. (2018). Probing the DPRK nuclear test site down to low-seismic magnitude. *Seismological Research Letters*, *89*, 2034–2041. https://dx.doi.org/10.1785/0220180116

Gibbons, S. J., Pabian, F., Näsholm, S. P., Kværna, T., & Mykkeltveit, S. (2017). Accurate relative location estimates for the North Korean nuclear tests using empirical slowness corrections. *Geophysical Journal International*, *208*(1), 101–117. https://doi.org/10.1093/gji/ggw379

Hartmann, G., Gestermann, N., & Ceranna, L. (2016). Seismological analysis of the fourth North Korean nuclear test. In EGU General Assembly Conference Abstracts (Vol. 18, p. EPSC2016-15713).

Haskell, N. A. (1967). Analytic approximation for the elastic radiation from a contained underground explosion. *Journal of Geophysical Research*, *72*, 2583–2587.

He, X., Zhao, L.-F., Xie, X.-B., & Yao, Z.-X. (2018). High-precision relocation and event discrimination for the 3 September 2017 underground nuclear explosion and subsequent seismic events at the North Korean test site. *Seismological Research Letters*, *89*(6), 2042–2048. https://doi.org/10.1785/0220180164

Helmberger, D. V., & Hadley, D. M. (1981). Seismic source functions and attenuation from local and teleseismic observations of the NTS events Jorum and Hadley. *Bulletin of the Seismological Society of America*, *71*, 51–67.

Ichinose, G. A., Myers, S. C., Ford, S. R., Pasyanos, M. E., & Walter, W. R. (2017). Relative surface wave amplitude and phase anomalies from the Democratic People's Republic of Korea announced nuclear tests. *Geophysical Research Letters*, *44*, 8857–8864. https://doi.org/10.1002/2017GL074577

Kennett, B. L. N., & Engdahl, E. R. (1991). Travel times for global earthquake location and phase association. *Geophysical Journal International*, *105*, 429–465.

Lay, T. (1985). Estimating explosion yield by analytical waveform comparison. *Geophysical Journal of the Royal Astronomical Society*, *82*, 1–30.

Lay, T., Burdick, L. J., & Helmberger, D. V. (1984). Estimating the yields of the Amchitka tests by waveform intercorrelation. *Geophysical Journal of the Royal Astronomical Society*, *78*, 181–207.

Liu, J., Li, L., Zahradnik, J., Sokos, E., Liu, C., & Tian, X. (2018). North Korea's 2017 test and its nontectonic aftershock. *Geophysical Research Letters*, *45*, 3017–3025. https://doi.org/10.1002/2018GL077095

Liu, J., Li, L., Zahradník, J., Sokos, E., & Plicka, V. (2018). Generalized source model of the North Korea tests 2009–2017. *Seismological Research Letters*, *89*(6), 2166–2173. https://doi.org/10.1785/0220180106

Mueller, R. A., & Murphy, J. R. (1971). Seismic characteristics of underground nuclear detonations Part I. Seismic spectrum scaling. *Bulletin of the Seismological Society of America*, *61*, 1675–1692.

Murphy, J. R., Stevens, J. L., Kohl, B. C., & Bennett, T. J. (2013). Advanced seismic analyses of the source characteristics of the 2006 and 2009 North Korean nuclear tests. *Bulletin of the Seismological Society of America*, *103*, 1640–1661.

Myers, S. C., Ford, S. R., Mellors, R. J., Baker, S., & Ichinose, G. (2018). Absolute locations of the North Korean nuclear tests based on differential seismic arrival times and InSAR. *Seismological Research Letters*, *89*(6), 2049–2058. https://doi.org/10.1785/0220180123

Ni, S., Helmberger, D., & Pitarka, A. (2010). Rapid source estimation from global calibrated paths. *Seismological Research Letters*, *81*, 498–504. https://dx.doi.org/10.1785/gssrl.81.3.498

Pabian, F., & Coblentz, D. (2018). Observed surface disturbances associated with the DPRK's 3 September 2017 underground nuclear test. *Seismological Research Letters*, *89*(6), 2017–2024. https://doi.org/10.1785/0220180120

Pabian, F., & Hecker, S. (2012). Contemplating a third nuclear test in North Korea, Bulletin of Atomic Science, August, https://thebulletin.org/2012/08/contemplating-a-third-nuclear-test-in-north-korea/ (last accessed November, 2018).

Pasyanos, M. E., & Myers, S. C. (2018). The coupled location/depth/yield problem for North Korea's declared nuclear tests. *Seismological Research Letters*, *89*(6), 2059–2067. https://doi.org/10.1785/0220180109

Patton, H. J., & Pabian, F. V. (2014). Comment on "Advanced seismic analyses of the source characteristics of the 2006 and 2009 North Korean nuclear tests" by J. R. Murphy, J. L. Stevens, B. C. Kohl, and T. J. Bennett. *Bulletin of the Seismological Society of America*, *104*(4), 2104–2110. https://doi.org/10.1785/0120130262

Rodgers, A. J., Petersson, N. A., & Sjogreen, B. (2010). Simulation of topographic effects on seismic waves from shallow explosions near the North Korean nuclear test site with emphasis on shear wave generation. *Journal of Geophysical Research*, *115*, B11309. https://dx.doi.org/10.1029/2010JB007707

Rougier, E., Patton, H. J., Knight, E. E., & Bradley, C. R. (2011). Constraints on burial depth and yield of the 25 May 2009 North Korean test from hydrodynamic simulations in a granite medium. *Geophysical Research Letters*, *38*, L16316. https://doi.org/10.1029/2011GL048269

Saikia, C. K. (2017). Time-domain source function (TDSF) for nuclear and chemical explosions—Analysis around Nevada National Security Site (NNSS). *Geophysical Journal International*, *209*, 1048–1063. https://doi.org/10.1093/gji/ggx072

Selby, N. K. (2010). Relative locations of the October 2006 and May 2009 DPRK announced nuclear tests using International Monitoring System seismometer arrays. *Bulletin of the Seismological Society of America*, *100*, 1779–1784. https://doi.org/10.1785/0120100006

Sinha, R. S. (1991). *Underground structures: Design and construction*. New York, New York: Elsevier Science Publishing Company.

Stevens, J. L., & Day, S. M. (1985). The physical basis of m_b: M_S and variable frequency magnitude methods for earthquake/explosion discrimination. *Journal of Geophysical Research*, *90*, 3009–3020.

Stevens, J. L., & O'Brien, M. (2018). 3D nonlinear calculation of the 2017 North Korean nuclear test. *Seismological Research Letters*, *89*, 2068–2077. https://doi.org/10.1785/0220180099

Stroujkova, A. (2018). Extracting the source spectra for the North Korean nuclear tests. *Seismological Research Letters*, *89*(6), 2174–2182. https://doi.org/10.1785/0220180125

Vavrycuk, V., & Kim, S. G. (2014). Nonisotropic radiation of the 2013 North Korean nuclear explosion. *Geophysical Research Letters*, *41*, 7048–7056. https://doi.org/10.1002/2014GL061265

von Seggern, D., & Blandford, R. (1972). Source time functions and spectra for underground nuclear explosions. *Geophysical Journal of the Royal Astronomical Society*, *31*, 83–97.

Walter, W. R., Dodge, D. A., Ichinose, G., Myers, S. C., Pasyanos, M. E., & Ford, S. R. (2018). Body-wave methods of distinguishing between explosions, collapses, and earthquakes: Application to recent events in North Korea. *Seismological Research Letters*, *89*(6), 2131–2138. https://doi.org/10.1785/0220180128

Walter, W. R. & Ford, S. R. (2018). A preliminary explosion seismic spectral model for saturated/hard rock, *Tech. Rept. LLNL-TR-754292*, Lawrence Livermore National Laboratory, Livermore, California, 14 pp.

Walter, W. R., & Priestley, K. F. (1991). High-frequency *P* wave spectra from explosions and earthquakes. In *Explosion source phenomenology*, *Geophysical Monograph* (Vol. 65, pp. 219–228). Washington, DC: American Geophysical Union.

Wang, T., Shi, Q., Nikkhoo, M., Wei, S., Barbot, S., Dreger, D., et al. (2018). The rise, collapse, and compaction of Mt. Mantap from the 3 September 2017 North Korean nuclear test. *Science*, *361*, 166–170. https://doi.org/10.1126/science.aar7230

Wei, M. (2017). Location and source characteristics of the 2016 January 6 North Korean nuclear test constrained by InSAR. *Geophysical Journal International*, *209*(2), 762–769. https://doi.org/10.1093/gji/ggx053

Wen, L. X., & Long, H. (2010). High-precision location of North Korea's 2009 nuclear test. *Seismological Research Letters*, *81*(1), 26–29. https://dx.doi.org/10.1785/gssrl.81.1.26

Yao, J., Tian, D., Sun, L., & Wen, L. (2018). Source characteristics of North Korea's 3 September 2017 nuclear test. *Seismological Research Letters*, *89*(6), 2078–2084. https://doi.org/10.1785/0220180134

Zhang, M., & Wen, L. (2013). High-precision location and yield of North Korea's 2013 nuclear test. *Geophysical Research Letters*, *40*, 2941–2946. https://doi.org/10.1002/grl.50607

Zhao, L.-F., Xie, X.-B., He, X., Zhao, X., & Yao, Z.-X. (2017). Seismological discrimination and yield estimation of the 3 September 2017 Democratic People's Republic of Korea (DPRK) underground nuclear test. *Science China Bulletin*, *62*, 4163–4168.

Zhao, L.-F., Xie, X.-B., Wang, W., Fan, N., Zhao, X., & Yao, Z.-X. (2017). The 9 September 2016 North Korean underground nuclear test. *Bulletin of the Seismological Society of America*, *107*(6), 3044–3051. https://doi.org/10.1785/0120160355

Zhao, L.-F., Xie, X.-B., Wang, W.-M., Hao, J.-L., & Yao, Z.-X. (2016). Seismological investigation of the 2016 January 6 North Korean underground nuclear test. *Geophysical Journal International*, *206*(3), 1487–1491. https://dx.doi.org/10.1093/gji/ggw239

Zhao, L. F., Xie, X.-B., Wang, W.-M., & Yao, Z.-X. (2008). Regional seismic characteristics of the 9 October 2006 North Korean nuclear test. *Bulletin of the Seismological Society of America*, *98*, 2571–2589. https://dx.doi.org/10.1785/0120080128

Zhao, L.-F., Xie, X.-B., Wang, W.-M., & Yao, Z.-X. (2012). Yield estimation of the 25 May 2009 North Korean nuclear explosion. *Bulletin of the Seismological Society of America*, *102*, 467–478. https://doi.org/10.1785/0120110163

Zhao, L.-F., Xie, X.-B., Wang, W.-M., & Yao, Z.-X. (2014). The 12 February 2013 North Korean underground nuclear test. *Seismological Research Letters*, *85*, 130–134. https://doi.org/10.1785/0220130103

References From the Supporting Information

Koper, K. D., Herrmann, R. B., & Benz, H. M. (2008). Overview of open seismic data from the North Korean event of 9 October 2006. *Seismological Research Letters*, *79*, 178–185. https://dx.doi.org//10.1785/gssrl.79.2.178